

AD A 044206

AFGL-TR-77-0117

NEAR FIELD PATTERNS OF SEISMIC RADIATION

Robert L. Kovach
Moshe Israel

Department of Geophysics
Stanford University
Stanford, California 94305

31 May 1977

Final Report for Period 19 February 1976 - 18 May 1977

Approved for public release; distribution unlimited

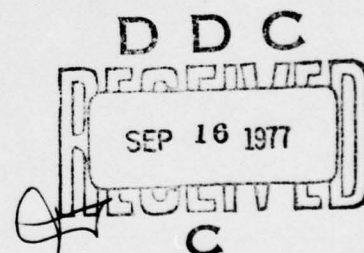
Sponsored by:

Defense Advanced Research Projects Agency
ARPA Order No. 1795, Amendment 11.

Monitored by:

AIR FORCE GEOPHYSICS LABORATORY
AIR FORCE SYSTEMS COMMAND
UNITED STATES AIR FORCE
HANSCOM AFB, MASSACHUSETTS 01731

AD No. /
DDC FILE COPY



Under Contract No. F19628-76-C-0143
Effective Date of Contract: 19 February 1976
Contract Expiration Date: 18 May 1977
Principal Investigator: R.L. Kovach

The views and conclusions contained in this document are those of the authors and should not be interpreted as necessarily representing the official policies, either expressed or implied, of the Defense Advanced Research Projects Agency or the U.S. Government.

Qualified requestors may obtain additional copies from the Defense Documentation Center. All others should apply to the National Technical Information Service.

Unclassified

SECURITY CLASSIFICATION OF THIS PAGE (When Data Entered)

REPORT DOCUMENTATION PAGE		READ INSTRUCTIONS BEFORE COMPLETING FORM
1. REPORT NUMBER AFGL-TR-77-0117	2. GOVT ACCESSION NO.	3. RECIPIENT'S CATALOG NUMBER
4. TITLE (and Subtitle) NEAR FIELD PATTERNS OF SEISMIC RADIATION		5. TYPE OF REPORT & PERIOD COVERED Final Report 2/19/76-5/18/77 19 Feb 75 - 18 May 73
7. AUTHOR(s) Robert L. Kovach and Moshe Israel		6. PERFORMING ORG. REPORT NUMBER
9. PERFORMING ORGANIZATION NAME AND ADDRESS Department of Geophysics Stanford University Stanford, California 94305		8. CONTRACT OR GRANT NUMBER(s) F19628-76-C-0143 MAR 1976 Order - 1795
11. CONTROLLING OFFICE NAME AND ADDRESS Air Force Geophysics Laboratory (AFSC) Hanscom AFB, Massachusetts 01731 Monitor/Ker C. Thomson/LW		10. PROGRAM ELEMENT, PROJECT, TASK AREA & WORK UNIT NUMBERS 62701E ARPA Order No. 179 5
14. MONITORING AGENCY NAME & ADDRESS (if diff. from Controlling Office)		12. REPORT DATE 31 May 1977
		13. NO. OF PAGES 58
		15. SECURITY CLASS. (of this report) Unclassified
		15a. DECLASSIFICATION/DOWNGRADING SCHEDULE
16. DISTRIBUTION STATEMENT (of this report) Approved for public release; distribution unlimited		
17. DISTRIBUTION STATEMENT (of the abstract entered in Block 20, if different from report)		
18. SUPPLEMENTARY NOTES This research was sponsored by the Defense Advanced Research Projects Agency. ARPA Order No. 1795		
19. KEY WORDS (Continue on reverse side if necessary and identify by block number) Near field motions. Theoretical seismograms. Ground motion.		
20. ABSTRACT (Continue on reverse side if necessary and identify by block number) Near field displacement, velocity and acceleration ground motion are computed for a buried finite strike slip fault using generalized multipolar ray theory to study the effects of rupture velocity, rise time of particle displacement, direction of rupture relative to observing station and the presence of the free surface. Computed displacement seismograms demonstrate that the rise time and rupture velocity can be traded off to produce similar wave shapes emphasizing the difficulty of separating the effects of rise		

DD FORM 1 JAN 73 1473

EDITION OF 1 NOV 65 IS OBSOLETE

Unclassified

SECURITY CLASSIFICATION OF THIS PAGE (When Data Entered)

Unclassified

SECURITY CLASSIFICATION OF THIS PAGE (When Data Entered)

19. KEY WORDS (Continued)

20. ABSTRACT (Continued)

time and rupture velocity can be traded off to produce similar wave shapes emphasizing the difficulty of separating the effects of rise time and rupture velocity. On the other hand, synthetic accelerograms exhibit much character as the rise time becomes a small part of the rupture duration and individual contributions to the acceleration signals such as the P- and S-wave stopping phase can be seen. Near field synthetic accelerograms hold promise for the study of fault rupture parameters. For the strike-slip model studied allowance for the presence of a free surface by doubling of the amplitude of infinite space signals seems to be approximately correct even in the case of computed vertical component accelerograms. However, this result is not generally true for the residual static displacements. The known result of the appearance of Rayleigh waves at horizontal distances greater than five times the source depth is confirmed for dislocation sources. A portion of the near-field coda can be attributed to the presence of crustal layers which must be accurately known before the source radiation can be completely known.

Unclassified

SECURITY CLASSIFICATION OF THIS PAGE (When Data Entered)

TABLE OF CONTENTS

	<u>Page</u>
PREFACE	1
LIST OF ILLUSTRATIONS	2
INTRODUCTION	5
THEORY	7
NUMERICAL RESULTS	17
CONCLUSIONS	25
REFERENCES	26
PUBLISHED PAPERS	28
APPENDIX	47

Section <input checked="" type="checkbox"/>	
Section <input type="checkbox"/>	
Section <input type="checkbox"/>	
DISTRIBUTION CODES	
SPECIAL	
A	

PREFACE

The research discussed in this report had several objectives: 1) an examination of the effect of the free surface on the near-field seismic radiation for seismic sources imbedded in an elastic half-space; 2) an examination of the interrelation of various parameters such as source dimension, rise time and frequency and 3) an examination of the effects of fault length and rupture velocity in the near-field together with a study of the near-field coda.

LIST OF ILLUSTRATIONS

- FIGURE 1. Assumed fault model and location of observing stations.
- FIGURE 2. Transverse component of displacement U_3 at Stations A and D. Amplitude is given in terms of the assumed U_0 in cm divided by 1000. τ is the rise time in seconds and v is the rupture velocity.
- FIGURE 3. Transverse component of displacement U_3 at stations A1 and D1. A1 and D1 are located at distances less than the critical distance of the SP head wave.
- FIGURE 4. Three components of displacement at Station B located in the SW quadrant in the direction of fault rupture.
- FIGURE 5. Three components of displacement at station C located in the NW quadrant behind the direction of fault rupture.
- FIGURE 6. Displacement seismograms at stations B and C which illustrate the effect of varying the rupture velocity for fixed source rise times of 0.5 and 1.0 seconds.
- FIGURE 7. Displacement seismograms at stations B1 and C1 for various rupture parameters.
- FIGURE 8. Vertical component of displacement at stations B and C for various rupture parameters.
- FIGURE 9. Vertical component of particle velocity at station B for various rupture parameters. Note the increase in amplitude as the rupture velocity approaches the shear velocity (3.2 km/sec) of the medium.
- FIGURE 10. Vertical component of particle acceleration at station B for a source rise time of 0.5 seconds. Note the appearance of the P and S wave stopping phases.

- FIGURE 11. Vertical component of particle acceleration at station B for a source rise time of 1.0 seconds. Wave character is simpler than in Figure 10 and individual stopping phases are not recognizable since the source time is comparable to the fault length divided by the rupture velocity.
- FIGURE 12. Vertical component of particle acceleration at station C. Note the distinct stopping phases.
- FIGURE 13. Vertical component of displacement for a buried strike-slip source at two epicentral distances.
- FIGURE 14. Radial component of displacement for a buried strike-slip source at increasing epicentral distances. Note appearance of Rayleigh pulse.
- FIGURE 15. Radial component of displacement for a buried dip-slip source at increasing epicentral distances. The seismogram for $r = 100$ km begins at 16.5 seconds and has been offset to avoid overlapping seismogram at $r = 50$ km. Amplitude scales are identical.
- FIGURE 16. Radial component of displacement for a dip-slip source at increasing epicentral distances. Note enhancement of Rayleigh pulse due to shallower depth of source as compared to Figure 15. Seismogram at $r = 5$ km utilizes displacement scale ranging from 0 to -20 microns. Seismograms at 10, 20, 50 and 100 km are plotted at same amplitude scale utilizing scale next to $r = 10$ km. Seismogram at $r = 100$ km begins at 16.5 seconds and slightly overlaps end of $r = 50$ km seismogram.
- FIGURE 17. Observed and computed near-field seismograms for a central California earthquake. A is the fault area and \bar{u} is the average dislocation. Different values of $A\bar{u}$ are estimated on opposite

sides of the fault presumably due to the effect of geology at the recording sites. SAGO-East is situated on Pliocene sediments whereas SAGO-Central is located on granite. Larger amplitudes are commonly observed on sediments relative to bedrock.

FIGURE 18. Theoretical point source seismograms.

- a) Homogeneous half-space.
- b) Layered half-space. Source depth 12.5 km, epicentral distance 5 km.

INTRODUCTION

Observations have recently been made with broadband displacement transducers recording within a few source depths, source dimensions or wavelengths of central California earthquakes (Johnson and McEvilly, 1974). At these short distances, where hopefully the effects of scattering and attenuation are minimized, one hopes to gain insight into details of the faulting mechanism, such as rupture velocity and the time function of displacement.

Our motivation for computing theoretical seismograms is to gain some insight into the effects of the free surface, and rupture parameters for a propagating strike-slip fault in the near-field. Specification of a working model and its resultant theoretical seismogram, which can be compared to observed data, is an important facet in our ability to predict strong ground motion in the near field of potentially damaging earthquakes.

Near-field displacements have been examined using dislocation modeling in an infinite space (Haskell, 1969; Kanamori, 1972; Trifunac, 1974; Trifunac and Udawadia, 1974; Anderson, 1974; Anderson and Richards, 1975). The effect of a free surface on near-field displacements has been examined by Kawaski et al. (1973) and Kawasaki and Suzuki (1974). Anderson (1976) has examined the near-field motions due to a shallow rupturing fault using a Green's function which is a solution to Lamb's problem. Anderson's paper critically discusses the conditions under which the free surface may be reasonably accounted for by doubling the amplitude of motions in an infinite space. In particular, the SH motions from a strike-slip source and the P-SV motions from a dip-slip source were examined. Archuleta and Frazier (1976) have

utilized a three-dimensional finite element approach to examine particle displacements and velocities in the near field for propagating shear fractures.

In this research, we have made use of the generalized multipolar ray theory (GMRT) advocated by Ben-Menahem and Vered (1973) to examine the near-field motions of a propagating strike-slip fault. GMRT is a comprehensive theory adaptable to the computation of both near-field and far-field theoretical seismograms utilizing surface or buried dislocation sources. The theory also permits, under certain conditions, the computation of ground velocity and acceleration.

THEORY

We adopt a cartesian coordinate system in which the free surface of a homogeneous half space is represented by the xy plane. In the xz plane we define a rectangular fault surface

$$0 \leq x \leq L$$

$$H_1 \leq z \leq H_2$$

Displacement occurs such that all points of the rectangle having the same coordinate x move simultaneously, i.e. a line source with a width $h = H_2 - H_1$ moves along the xz plane.

It has been shown by Ben-Menahem and Vered (1973) that the Laplace transformed surface displacements of each component due to a dislocation point source located at $(0,0,H)$ are given by expressions of the form

$$\bar{U} = \frac{1}{r^N} \left\{ \begin{array}{l} \cos M\phi \\ \sin M\phi \end{array} \right\} s^n \int_0^\infty J_m(su) u^{2\ell+m+1} f(u^2) \exp\left[-s\left(u^2 + \frac{1}{c^2}\right)^{1/2} H\right] du \quad (1)$$

ℓ , n , m , N and M are source dependent integer constants. r is the epicentral distance, ϕ is the azimuthal angle, c is the elastic wave propagation velocity, s is the Laplace parameter, u is an integration variable and $f(u^2)$ is a function of u^2 . A step-like source time function is initially assumed at the source, i.e., $U_0(s) = U_0 s^{-1}$.

The depth of the source, H , appears only in the exponent in (1). Thus, using the principle of superposition, the Laplace-transformed displacement generated by a line source which is composed of point sources continuously distributed along an interval $h = H_2 - H_1$, is given by the expression

$$\int_{H_1}^{H_2} \bar{U} dH = \frac{1}{r^N} s^{n-1} \left\{ \frac{\cos M\phi}{\sin M\phi} \right\} \int_0^\infty J_m(\text{sur}) u^{2\ell+m+1} \frac{f(u^2)}{(u^2 + \frac{1}{c^2})^{1/2}} \cdot \left\{ \exp[-s(u^2 + \frac{1}{c^2})^{1/2} H_1] - \exp[-s(u^2 + \frac{1}{c^2})^{1/2} H_2] \right\} du \quad (2)$$

We denote by \bar{U}_z , \bar{U}_r and \bar{U}_ϕ the vertical, radial and azimuthal components of displacement. From Table 2 in Ben-Menahem and Vered (1973) and (2) we obtain

$$\bar{U}_z = \frac{dx \sin 2\phi}{4\pi} U_0 \int_0^\infty \frac{\Gamma_2}{\Delta} \left(\frac{b'}{a} E_a - a E_b \right) du \quad (3)$$

$$\bar{U}_\phi = \frac{dx \cos 2\phi}{2\pi} U_0 \int_0^\infty \left\{ \frac{\Gamma_2}{sr\Delta} \left(\frac{b}{a} E_a + \frac{P}{b^2} E_b \right) - \frac{\Gamma_1}{b^2} E_b \right\} du \quad (4)$$

$$\bar{U}_r = \frac{-dx \sin 2\phi}{4\pi} U_0 \int_0^\infty \left\{ \frac{2\Gamma_2}{sr\Delta} \left(\frac{b}{a} E_a + \frac{P}{b^2} E_b \right) + \frac{\Gamma_1}{\Delta} (b' E_b - \frac{u^2 b}{a} E_a) \right\} du \quad (5)$$

where

$$E_a = [e^{-saH_1} - e^{-saH_2}]$$

$$E_b = [e^{-sbH_1} - e^{-sbH_2}]$$

$$\Gamma_m = u^{m+1} J_m(\text{sur})$$

$$P = [b' - 2ab]$$

$$\Delta = b'^2 - u^2 ab$$

$$a = (u^2 + 1/\alpha^2)^{1/2}$$

$$b = (u^2 + 1/\beta^2)^{1/2}$$

$$b' = (u^2 + 1/2\beta^2)$$

The longitudinal and shear wave velocities are denoted by α and β respectively.

The time domain solution is obtained by the method of Cagniard-Pekeris for dislocation sources. As an example we will treat the radial component of motion. We first write (5) in the form

$$\bar{U}_r = \bar{U}_{r,p_1} + \frac{1}{s} \bar{U}_{r,p_2} + \bar{U}_{r,s_1} + \frac{1}{s} \bar{U}_{r,s_2} \quad (6)$$

where

$$\bar{U}_{r,p_1} = \frac{dx \sin 2\phi}{4\pi} U_0 \int_0^\infty \frac{\Gamma_1 u^2 b}{a\Delta} E_a du \quad (7)$$

$$\bar{U}_{r,p_2} = \frac{-dx \sin 2\phi}{2\pi r} U_0 \int_0^\infty \frac{\Gamma_2 b}{a\Delta} E_a du \quad (8)$$

$$\bar{U}_{r,s_1} = \frac{-dx \sin 2\phi}{4\pi} U_0 \int_0^\infty \frac{\Gamma_1 b'}{\Delta} E_b du \quad (9)$$

$$\bar{U}_{r,s_2} = \frac{-dx \sin 2\phi}{2\pi r} U_0 \int_0^\infty \frac{\Gamma_2^P}{b^2 \Delta} E_b du \quad (10)$$

We next perform the time domain inversion of (7)-(10) using equations (42) and (53)-(57) from

Ben-Menahem and Vered (1973).

$$U_{r,p_1} = \frac{\sin 2\phi}{2\pi^2 r} \frac{U_0 dx}{H(t-\tau_p) \text{Im}} \int_{\tau_p}^t \frac{bv^3(t-\tau+vr)d\tau}{[(\tau_p+\tau)(t-\tau+2vr)]^{1/2} [(\tau_p-\tau)(t-\tau)]^{1/2}} \quad (11)$$

$$U_{r,p_2} = \frac{\sin 2\phi}{\pi^2 r^3} \frac{U_0 dx}{H(t-\tau_p) \text{Im}} \int_{\tau_p}^t \frac{v[2(t-\tau)(t-\tau+2vr) + v^2 r^2] d\tau}{[(\tau_p+\tau)(t-\tau+2vr)]^{1/2} [(\tau_p-\tau)(t-\tau)]^{1/2}} \quad (12)$$

$$U_{r,s_1} = \frac{\sin 2\phi}{2\pi^2 r} \frac{U_0 dx}{H(t-\tau_{bs}) \text{Im}} \int_{\tau_{bs}}^t \frac{vbb'(t-\tau+vr)d\tau}{\Delta[(\tau_s+\tau)(t-\tau+2vr)]^{1/2} [(\tau_s-\tau)(t-\tau)]^{1/2}} \quad (13)$$

$$U_{r,s_2} = \frac{\sin 2\phi}{\pi^2 r^3} \frac{U_0 dx}{H(t-\tau_{bs}) \text{Im}} \int_{\tau_{bs}}^t \frac{vp[2(t-\tau)(t-\tau+2vr) + v^2 r^2] d\tau}{b\Delta[(\tau_s+\tau)(t-\tau+2vr)]^{1/2} [(\tau_s-\tau)(t-\tau)]^{1/2}} \quad (14)$$

where

$$v^2 = -u^2$$

$$v = \frac{\tau r}{R^2} - \frac{H}{R^2} \left(\frac{R^2}{C^2} - \tau^2 \right)^{1/2}, \quad \tau < \frac{R}{C}$$

$$v = \frac{\tau r}{R^2} + \frac{iH}{R^2} \left(\tau^2 - \frac{R^2}{C^2} \right)^{1/2}, \quad \tau > \frac{R}{C}$$

$$R^2 = r^2 + H^2$$

$$C = \alpha \text{ or } \beta$$

$$\tau_{bs} = \min \left[\frac{R}{\beta}, \frac{r}{\alpha} + H \left(\frac{1}{\beta^2} - \frac{1}{\alpha^2} \right)^{1/2} \right]$$

$$\tau_p = R/\alpha$$

$$\tau_s = R/\beta$$

$$f(H) \Big|_{H_2}^{H_1} = f(H_1) - f(H_2)$$

From (6) we thus obtain

$$U_r(t) = U_{r,p_1}(t) + \int_0^t U_{r,p_2}(\tau) d\tau + U_{r,s_1}(t) + \int_0^t U_{r,s_2}(\tau) d\tau \quad (15)$$

Equation (15) gives the ground displacement due to a step function U_0 .

For a continuous source function $U_0 g(t)$ we denote the ground displacement by $G_r(t)$. $G_r(t)$ is given by

$$G_r(t) = \int_0^t U_r(t-\tau)g'(\tau)d\tau \quad (16)$$

$$G_r(t) = \int_0^t U_r'(\tau)g(t-\tau)d\tau \quad (17)$$

From (15)-(17) we obtain

$$G_r(t) = \int_0^t \{ [U_{r,p_1}(\tau) + U_{r,s_1}(\tau)]g'(t-\tau) + [U_{r,p_2}(\tau) + U_{r,s_2}(\tau)]g(t-\tau) \} d\tau \quad (18)$$

By assuming that $g(t)$ has first and second continuous derivatives we can obtain ground velocity and acceleration by differentiating (18):

$$G_r'(t) = \int_0^t \{ [U_{r,p_1}(\tau) + U_{r,s_1}(\tau)]g''(t-\tau) + [U_{r,p_2}(\tau) + U_{r,s_2}(\tau)]g'(t-\tau) \} d\tau \quad (19)$$

$$G_r''(t) = \int_0^t \{ U_{r,p_1}(\tau) + U_{r,s_1}(\tau)g'''(t-\tau) + [U_{r,p_2}(\tau) + U_{r,s_2}(\tau)]g''(t-\tau) \} d\tau \quad (20)$$

Table 1 gives the necessary change of variables to evaluate the integrals in (11)-(14). Calculated seismograms for the infinite media can be accomplished by a slight change of the integrands in (11)-(14).

Table 1

Integral Transformations

$$U_{r,p_1}, U_{r,p_2}$$

$$q = \sin^{-1} \left(\frac{t - \tau_p}{t - \tau_p} \right)^{1/2}$$

$$U_{r,s_1}, U_{r,s_2}$$

$$I \quad r < r_c$$

$$r_c = H / \left(\frac{\alpha}{\beta} - 1 \right)^{1/2}$$

$$q = \sin^{-1} \left(\frac{t - \tau_s}{t - \tau_s} \right)^{1/2}$$

$$II \quad r > r_c$$

$$t < \tau_s$$

$$q = \sin^{-1} \left(\frac{\tau_s}{t} \right)^{1/2}$$

$$III \quad r > r_c$$

$$t > \tau_s$$

$$\text{write} \quad \int_{\tau_{bs}}^t = \int_{\tau_{bs}}^{\tau_s} + \int_{\tau_s}^t$$

$$\int_{\tau_{bs}}^{\tau_s}$$

$$q = \sin^{-1} \left(\frac{\tau_s}{\tau_s} \right)^{1/2}$$

$$\int_{\tau_s}^t$$

$$q = \sin^{-1} \left(\frac{t - \tau_s}{t - \tau_s} \right)^{1/2}$$

To obtain seismograms for a finite source, we next divide the length of the fault L into equal subintervals δL_i ($i = 1, \dots, r$). For every subinterval, the corresponding time function $g(t)$ derived from expression (1) or (2) is computed for the selected azimuthal angle ϕ and epicentral distance r . The final signal is calculated by adding the signals corresponding to all the subintervals δL_i , taking into account the appropriate time delay. A source time function

$$g(t) = \begin{cases} 0 & t < 0, \\ \frac{t}{\tau} - \frac{1}{2\pi} \sin\left(\frac{2\pi}{\tau} t\right) & 0 \leq t \leq \tau, \\ 1 & t > \tau, \end{cases} \quad (21)$$

where τ is the adopted rise time is assumed. The total time of rupture is equal to $(L/v) + \tau$ where L is the fault length and v is the rupture velocity. The assumed source time function is basically a step function with rounded shoulders and it will be useful for purposes of discussion to define an effective rise time τ_e equal to 0.6τ . The effective rise time τ_e is simply the rise time of a ramp step function positioned along the time axis to approximate the response of the rounded step function.

The numerical results were checked by independently computing the static displacements for a buried strike-slip point source. In an elastic half-space the static displacements are given by the expressions (Ben-Menahem and Singh, 1968):

$$\begin{aligned} \bar{U}_z &= \frac{\Omega_1 \sin 2\phi}{R^2} A \tan^2 \frac{\psi}{2} \\ \bar{U}_r &= \frac{\Omega_1 \sin 2\phi}{R^2} [AW - B] \operatorname{cosec} \psi \tan^2 \frac{\psi}{2} \end{aligned} \quad (22)$$

$$\bar{U}_{\phi} = \frac{\Omega_1 \cos 2\phi}{R^2} [4\sigma - 2] \operatorname{cosec} \psi \tan^2 \frac{\psi}{2}$$

where $\Omega_1 = U_0 dS/4\pi$,

U_0 = amount of dislocation,

dS = fault area,

ψ = angle between vertical axis through source and radius vector
to point of observation,

$W = \cos \psi$

σ = Poisson's ratio,

$A = [3(1+W)^2W - (1-2\sigma)(2+W)]$,

$B = [3(1+W)^2 - (1-2\sigma)]$.

The static displacements in an infinite space can be derived by making use of the Laplace transform relation

$$\lim_{t \rightarrow \infty} U(t) = \lim_{s \rightarrow 0} s \bar{U}(s)$$

$$\bar{U}_z = \frac{3\Omega_1 \sin 2\phi}{4(1-\sigma)R^2} \cos \psi \tan^2(\psi/2)(1 + \cos \psi)^2,$$

$$\bar{U}_r = \frac{\Omega_1 \sin 2\phi}{4(1-\sigma)R^2} (3 \cos^2 \psi + 4\sigma - 5) \operatorname{cosec} \psi \tan^2(\psi/2)(1 + \cos \psi)^2 \quad (23)$$

$$\bar{U}_{\phi} = \frac{\Omega_1 \cos 2\phi}{2(1-\sigma)R^2} (2\sigma - 1) \operatorname{cosec} \psi \tan^2(\psi/2)(1 + \cos \psi)^2.$$

All displacement components for all sources tend to a limit, the so-called "residual deformation." In the near-field this limit is reached very soon after the arrival of the S-wave. Evaluation of the ratio of the half-space static displacements to those of the infinite space for

various angles ψ points out that the static displacements for an elastic half-space cannot in all cases be allowed for by simply doubling the infinite space displacements. This conclusion is in agreement with the results of Anderson (1976). A further check on the infinite space calculations was made using results obtained using the computer program developed by Boatright and Boore (1975).

NUMERICAL RESULTS

The coordinate system for the model assumed in this paper is shown in Figure 1. A P-wave velocity $\alpha = 5.5$ km/sec and an S-wave velocity $\beta = 3.2$ km/sec has been used throughout. A rectangular fault surface having an area of 3 km^2 is imbedded in an elastic half-space at a depth of 5 km. 5 km can be taken as a representative depth for California earthquakes. The fault plane is arbitrarily taken to lie in a N-S direction with rupture initiating at the northern end and propagating in a southerly direction ($-X_1$ axis). We shall be examining the U_1 , U_2 and U_3 components of the derived displacements, velocities and accelerations at various station locations. Stations A1 and A lie along the strike of the fault in the direction of rupture and stations B1 and B at an angle of 45° to the strike (azimuth 235°). Stations C1 and C are located at an azimuth of 325° and stations D1 and D are along the strike but behind the direction of rupture. In the results which follow seismograms are computed for rupture velocities of 2, 2.5 and 3 km/sec and source rise times τ of 0.5 and 1 seconds. The computed seismograms are given in units of $U_0/1000$ cm where U_0 is the assumed displacement on the fault.

We first proceed to examine the effect of the inclusion of a free surface. In Figure 2 we show theoretical seismograms for the transverse component of motion (U_3) at station A and D with and without the presence of the free surface. As can be seen the pulse shapes are similar and the peak to peak amplitudes are doubled when the free surface is included. This agrees well with theory for an incident SH component of motion. Figure 3 compares the transverse component of displacement at stations A1 and D1 located closer to the ends of the fault. At these locations the peak to peak amplitudes are only approximately doubled, ranging from a factor of 1.7 to 2, when the free

surface is included. Stations A1 and D1 are located at distances less than the critical distance for the existence of the SP head wave.

In Figures 4 and 5 we examine the effect of the presence of a free surface on the three components of displacement at stations B and C. As before the overall pulse shapes are quite similar and the main effect of the presence of the free surface is to increase the amplitude of the wave pulse. As before a factor of 2 increase in amplitude is a good approximation although in some instances, particularly for the vertical component of displacement U_2 , the difference in amplitudes is closer to a factor of 2.5. It thus appears, that for the strike-slip example presented here, allowance for a free surface by doubling the amplitude of the wave pulse computed for an infinite space is valid to within $\pm 25\%$ or so. Anderson (1976) has pointed out that the SV contribution to the displacement is strongly influenced by the presence of the free surface, depending on the angle of incidence, and is particularly emphasized with a dip-slip source.

As can be seen in Figures 2-5 the static displacements computed with the presence of a free surface differ by a factor of 1 to approximately 2 times the infinite space static displacements depending on the component of motion and the station location. It can be demonstrated using the expressions given by (22-23) that this is indeed the expected result, i.e., the static displacements cannot in all cases be allowed for by simply doubling the infinite space displacements.

Figures 6, 7 and 8 show displacement seismograms computed at stations B, C, B1 and C1 which compare the effects of varying the rupture velocity for fixed source rise times of 0.5 and 1.0 seconds. The effect of a free surface has been included. For a fixed source rise time increasing the rupture

velocity from 2 to 3 km/sec produces a small increase in amplitude and a slight decrease in the width of the wave pulse. This is to be expected inasmuch as the width of the pulse should be a function of the total time interval in which the fault is rupturing. If we define R_a as the distance from the edge in which rupture begins to the observing point the P-wave initial motion begins at R_a/α . The radiation from the source is completed at a time $\frac{L}{v} + \tau_e$; S-waves initiating at this moment will arrive at the point of observation at a time $\frac{L}{v} + \tau_e + R_b/\beta$ where R_b is the direct distance from the edge in which rupture is completed. The time

$$T = \frac{L}{v} + \tau_e + \frac{R_b}{\beta} - \frac{R_a}{\alpha} \quad (24)$$

seems to control the pulse width of the near-field seismograms computed here. The theoretical seismograms presented here all possess pulse widths* equal to T. Equation 24 describes the dependence of rise time, rupture velocity and the direction of rupture. The effect of the direction of rupture may be demonstrated by comparing seismograms at stations A and D and Al and Dl. For example, the difference in the value of T for stations D and A is about 1 second and for stations Dl and Al is about 0.6 second. This difference can be seen on the computed seismograms. The reason that the pulse width is simply T appears to result from the fact that the static displacement approximately achieves its final value soon after the arrival of the S-wave contributed from the segment in which the fracture is terminated. This will in general, however not always be true; for example, at larger distances where the emerging Rayleigh wave will contribute to a larger pulse width than that given by (24).

*For a point source the pulse width is equal to $\tau_e + R(\frac{1}{\beta} - \frac{1}{\alpha})$.

It may be noted that the terms L/v and τ_e in (24) are independent of the azimuth to the station. Thus, one may expect that different kinematical fault models possessing the same $L/v + \tau_e$ will result in the same pulse width. This implies that rupture velocity is not separable by examining the pulse width at stations of varying azimuths unless some connection that ties L/v and τ_e is assumed.

The displacement seismograms reveal that both the rise time and rupture velocity can be traded off to produce very similar wave shapes emphasizing that it would be difficult to separate the effects of rise time and rupture velocity using displacement seismograms. Any differences in displacement seismograms for various rupture parameters appear to be subtle except for an infinite rupture velocity where differences in rise time produce noticeable differences in the pulse shape, as shown in Figure 8. We therefore examined the vertical component of particle velocities and accelerations at stations B and C to evaluate their appropriateness for learning about details of the rupture process. One intuitively expects that more insight into the details of the faulting are carried in the high frequencies which are essentially filtered from displacement seismograms.

Figure 9 shows the vertical component of the particle velocities generated at station B for various combinations of rise time and rupture velocity. Here it can be noted that for a source rise time of 0.5 seconds increasing the rupture velocity from 2 to 3 km/sec produces significant changes in the amplitude and wave shape of the particle velocity pulse. In particular, the amplitude increases and the wave period (here taken as the peak to peak interval between wave maxima) decreases as the rupture velocity approaches that of the shear velocity (3.2 km/sec) of the medium.

For a slower rise time of 1.0 seconds the particle velocity pulses are somewhat simpler in character although the same gross effect can be seen. The comparison of particle velocities computed with and without the presence of a free surface reveal that even though the gross character of the velocity pulse appears similar one can note differences especially in the amplitude of the first positive upswing relative to the second upswing. However, if one compares peak to peak maximum particle velocities inclusion of a free surface produces an increase ranging from a factor of 2 to 2.3.

Figures 10 and 11 show the particle accelerations at station B for three different rupture velocities and source rise times of 0.5 and 1.0 seconds. The synthetic accelerograms exhibit much character and individual contributions to the acceleration signals such as the S-wave stopping phase (Savage, 1965) can be seen. For a source rise time of 0.5 seconds we have indicated the expected arrival time of the S-phase and the stopping phase of the S-wave. A small P-wave stopping phase can be recognized when the rupture velocity is 3 km/sec but cannot be noted for slower rupture velocities because its time of arrival occurs after the onset of the S-phase.

The accelerograms are much simpler in character when the rise time is increased to 1.0 second (Figure 11). In this case individual stopping phases are not obvious inasmuch as the rise time is comparable to the fault length divided by the rupture velocity, i.e., the fault is still radiating energy from near the initial point of rupture as the rupture reaches the end of the fault. Figure 12 shows accelerograms computed at station C located in the backward quadrant to the direction of rupture. In these accelerograms distinct P and S wave stopping phases can be noted.

The accelerograms presented here indeed emphasize that the adopted rise time of the source and the rupture velocity do play an important part in controlling the amplitude and overall shape of computed near-field accelerograms.

Whether synthetic accelerograms are justified in practice for comparison with observed accelerograms, however, would seem to depend on the azimuthal coverage of observations available, an assessment of the importance of layering and attenuation and whether enough fault parameters are independently known so that an appropriate kinematic model can be defined.

The near-field seismograms presented here have r/h ratios much less than 5 and there is no evidence of a Rayleigh wave. Pekeris and Lifson (1957) have shown for a buried point source that the Rayleigh pulse begins to emerge at $r/h = 5$ and is clearly recognizable at $r/h = 10$. To examine the applicability of this conclusion for a buried strike-slip source we computed the vertical and radial displacements at increasing epicentral distances (Figures 13 and 14). In these calculations a point source and a source rise time of 0.5 seconds were assumed together with a source potency $U_0 dS$ of 1×10^{-6} unit faults. (One unit fault = $1000 \text{ m} - \text{km}^2$ where dS is the fault area). As can be seen, a Rayleigh pulse is noticeable at $r/h = 5$. Similar results were obtained for a dip-slip* source (Figure 15). Figure 16 shows the effect of decreasing the depth of focus h for various distances r . Decreasing the depth of the source emphasizes the higher frequency components of the Rayleigh wave and a large Rayleigh pulse is prominent on the seismogram when $r/h \geq 50$. The conclusions of Pekeris and Lifson (1957), and amplified upon by Mooney (1974, 1976), thus also appear applicable to buried dislocation sources.

As a final example we examine observed near-field seismograms for a $M_L = 4.6$ earthquake recorded at SAGO-East and SAGO-Central as presented by Johnson and McEvilly (1974). In Figure 17 the signals shown represent actual recordings of ground displacement recorded at epicentral distances of 2.3

* Results for a dip-slip source can be derived using Table 2 in Ben-Menahem and Vered (1973).

km and 5.5 km. We do not attempt a detailed study of the source parameters of this earthquake but rather only demonstrate a fit of amplitudes and pulse widths based on several assumptions. A detailed study of this earthquake from a dynamic point of view is given by Israel and Vered (1977). First, the epicentral location was shifted by 0.75 km in the direction S 32° W in order to achieve agreement with the observed amplitudes at all stations. An adjustment of this amount is within the uncertainty of the epicenter location. Secondly, a fault area of 3 km² is assumed and rupture is taken to initiate at the focus and propagate to the southeast. A kinematic model is taken with a constant fault dislocation and a constant rupture velocity of 3 km/sec. The particle displacement is given by (21) and the rise time depends on the distance from the start of rupture according to

$$\tau = \frac{L-\ell}{L} \left(\frac{L}{v} \right)$$

where L is the fault length, here taken to be 3 km. The choice of fault kinematics is quite arbitrary and the theoretical seismograms shown in Figure 17, although quite satisfactory, are not unique.

A better azimuthal station distribution together with a model which incorporates the geological complexity of the area could possibly reduce the possible solutions. However, details of the rupture process are not resolvable from examination of only near field displacements.

As pointed out by McEvilly and Johnson (1974) the comparison of synthetic seismograms with actual seismograms provides a method for estimating the source moment in the time domain. The average source potency determined by comparison of the amplitude of the S-wave pulse with observations at SAGO-Central and SAGO-East is 185 cm-km². Converting to seismic moment,

assuming a rigidity of 2.73×10^{11} dynes/cm², yields a value of 5×10^{23} dyne-cm. With an assumed fault area of 3 km^2 this leads to an average dislocation U_0 of 61.7 cm. The computed seismic moment of 5×10^{23} dyne-cm agrees well with the value determined by Johnson and McEvilly (1974) assuming a point dislocation and the values obtained by Israel and Vered (1977) for a dynamical model of rupture, and points to the difficulty in extracting details of the rupture process from only examining near-field displacement data (Anderson and Richards, 1975). Near field synthetic accelerograms, however, hold some promise for the study of fault rupture parameters.

An attempt has also been made to examine what produces the coda in the seismic near field. Theoretical seismograms have been computed for a point source imbedded in a layered medium. An example of such a calculation is shown in Figure 18. Displayed are the seismograms for a vertical point source placed in a homogeneous half-space and in a layered half-space with parameters appropriate for the crustal structure near the San Andreas fault. The source depth was taken to be 12.5 km and the epicentral distance 5 km. Our computed seismograms demonstrate the general computational result that neither pulse amplitudes, nor pulse durations, are sensitive to crustal layering but that a portion of the near-field coda can be attributed to the presence of crustal layers and hence the receiver structure must be accurately known before the source radiation can be completely known.

CONCLUSIONS

Theoretical seismograms have been presented for a buried, propagating strike-slip fault to examine the effect of various rupture parameters and the presence of the free surface on the resulting particle displacement, velocity and acceleration at various azimuthal near-field locations. Rupture velocity and source rise time usually cannot be independently assessed on displacement seismograms inasmuch as the near-field pulse width is a function of fault length, rupture velocity, effective source rise time and the distances from the beginning and end of the rupture plane to the observing station. However, given a judicious (or fortuitous) azimuthal choice of observation points relative to a propagating strike-slip fault near-field synthetic accelerograms suggest some promise for the evaluation of fault rupture parameters. This could be of some importance in studying ground motions in the near-field of potentially damaging earthquakes.

For the strike-slip model discussed here, allowance for the presence of a free surface by doubling of the displacements, velocities and accelerations computed in an infinite space appears to be valid to within 25% or so. This conclusion is not generally valid in the case of the residual static displacements. A portion of the near-field coda can be directly attributed to the presence of crustal layers which must be accurately known before precise estimates of source parameters can be made.

REFERENCES

- Anderson, J.G. (1974) A dislocation model for the Parkfield earthquake, Bull. Seism. Soc. Amer., 64, 671-686.
- Anderson, J.G. (1976) Motions near a shallow rupturing fault: evaluation of effects due to the free surface, Geophys. J. R. Astr. Soc., 46, 575-593.
- Anderson, J.G. and P.G. Richards (1975) Comparison of strong ground motion from several dislocation models, Geophys. J. R. Astr. Soc., 43, 347-373.
- Archuleta, R.J. and G.A. Frazier (1976) Comparison of free surface, near-field ground motion for three, numerically simulated, strike-slip earthquakes, EOS, Trans. Amer. Geop. Union, 57, 952.
- Ben-Menahem, A. and S.J. Singh (1968) Eigenvector expansions of Green's dyads with applications to geophysical theory, Geophys. J.R. Astr. Soc., 16, 417-452.
- Ben-Menahem, A. and M. Vered (1973) Extension and interpretation of the Cagniard-Pekeris method for dislocation sources, Bull. Seism. Soc. Amer., 63, 1611-1636.
- Boatright, J. and D.M. Boore (1975) A simplification in the calculation of motions near a propagating dislocation, Bull. Seism. Soc. Amer., 65, 133-138.
- Haskell, N.A. (1969) Elastic displacements in the near-field of a propagating fault, Bull. Seism. Soc. Amer., 59, 865-908.
- Israel, M. and M. Vered (1977) Near-field source parameters by finite source theoretical seismograms, Bull. Seism. Soc. Amer., in press.
- Johnson, L.R. and T.V. McEvilly (1974) Near-field observations and source parameters of central California earthquakes, Bull. Seism. Soc. Amer., 64, 1855-1886.

- Kanamori, H. (1972) Determination of effective tectonic stress associated with earthquake faulting. The Tottori earthquake of 1943, Phys. Earth Planet. Int., 5, 426-434.
- Kawasaki, I. and Y. Suzuki (1974) Rise-time and effective stress estimation from comparison of near-field data with theoretical seismograms in a semi-infinite medium: Sanriku earthquake of March 3, 1933, J. Phys. Earth, 22, 223-236.
- Kawasaki, I., Y. Suzuki and R. Sato (1973) Seismic waves due to a shear fault in a semi-infinite medium, Part 1: point source, J. Phys. Earth, 21, 251-284.
- Mooney, H. (1974) Some numerical solutions for Lamb's problem, Bull. Seism. Soc. Am., 64, 473-491.
- Mooney, H. (1976) The seismic wave system from a surface impact, Geophysics, 41, 243-265.
- Pekeris, C. and H. Lifson (1957) Motion of the surface of a uniform half-space produced by a buried pulse, J. Acoust. Soc. Am., 29, 1233-1238.
- Savage, J.C. (1965) The stopping phase on seismograms, Bull. Seism. Soc. Amer., 55, 47-58.
- Trifunac, M.D. (1974) A three-dimensional dislocation model for the San Fernando, California, earthquake of February 9, 1971, Bull. Seism. Soc. Amer., 64, 149-172.
- Trifunac, M.D. & F.E. Udvardi (1974) Parkfield, California, earthquake of June 27, 1966: a three dimensional moving dislocation model, Bull. Seism. Soc. Amer., 64, 511-533.

PUBLISHED PAPERS

SUPPORTED BY CONTRACT F19628-76-C-0143

Vered, M., and A. Ben-Menahem, Generalized multipolar ray theory for surface and shallow sources, Geophys. J. Roy. Astr. Soc., 45, 195-198, 1976.

Ben-Menahem, A., The role of the shear Mach number in earthquake source dynamics, Bull. Seism. Soc. Amer., 66, 1787-1799, 1976.

Israel, M. and R. L. Kovach, Near field motions from a propagating strike slip fault in an elastic half-space, Bull. Seism. Soc. Amer., in press, August 1977 issue.

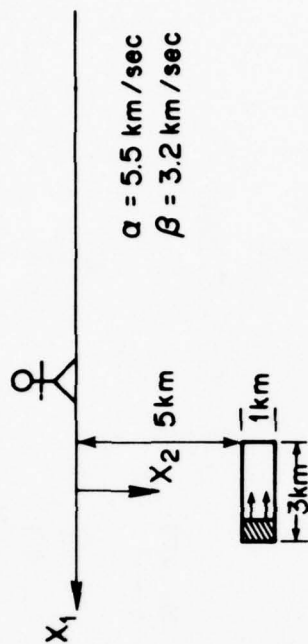
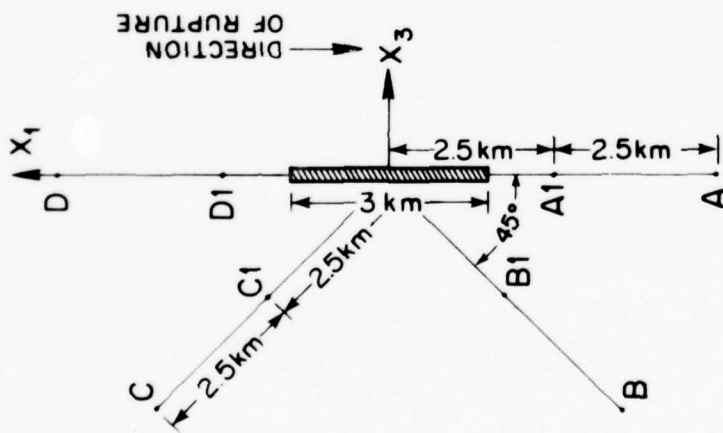


FIGURE 1

U_3 DISPLACEMENT

— INFINITE SPACE
 - - - HALF SPACE

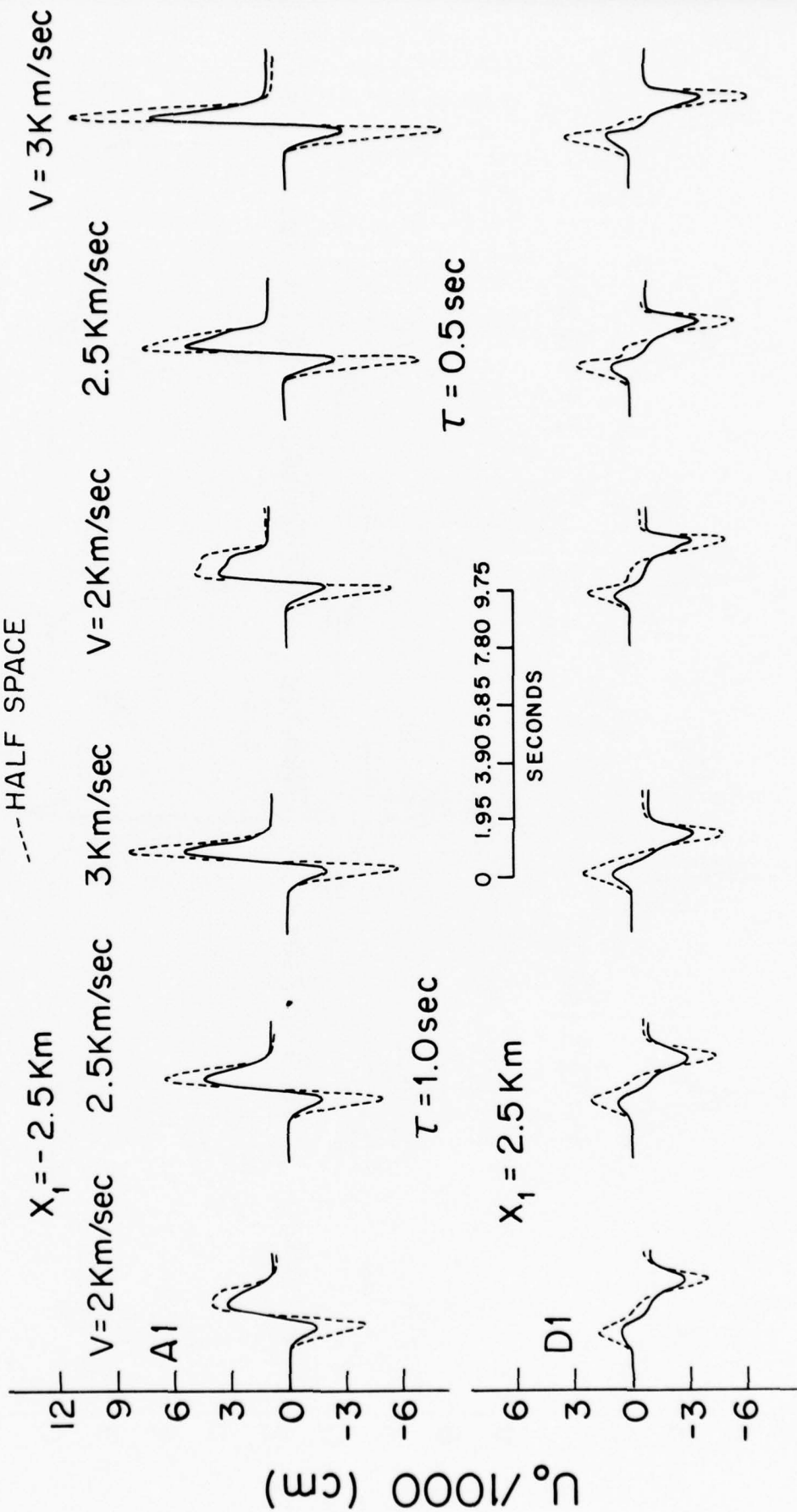


FIGURE 3

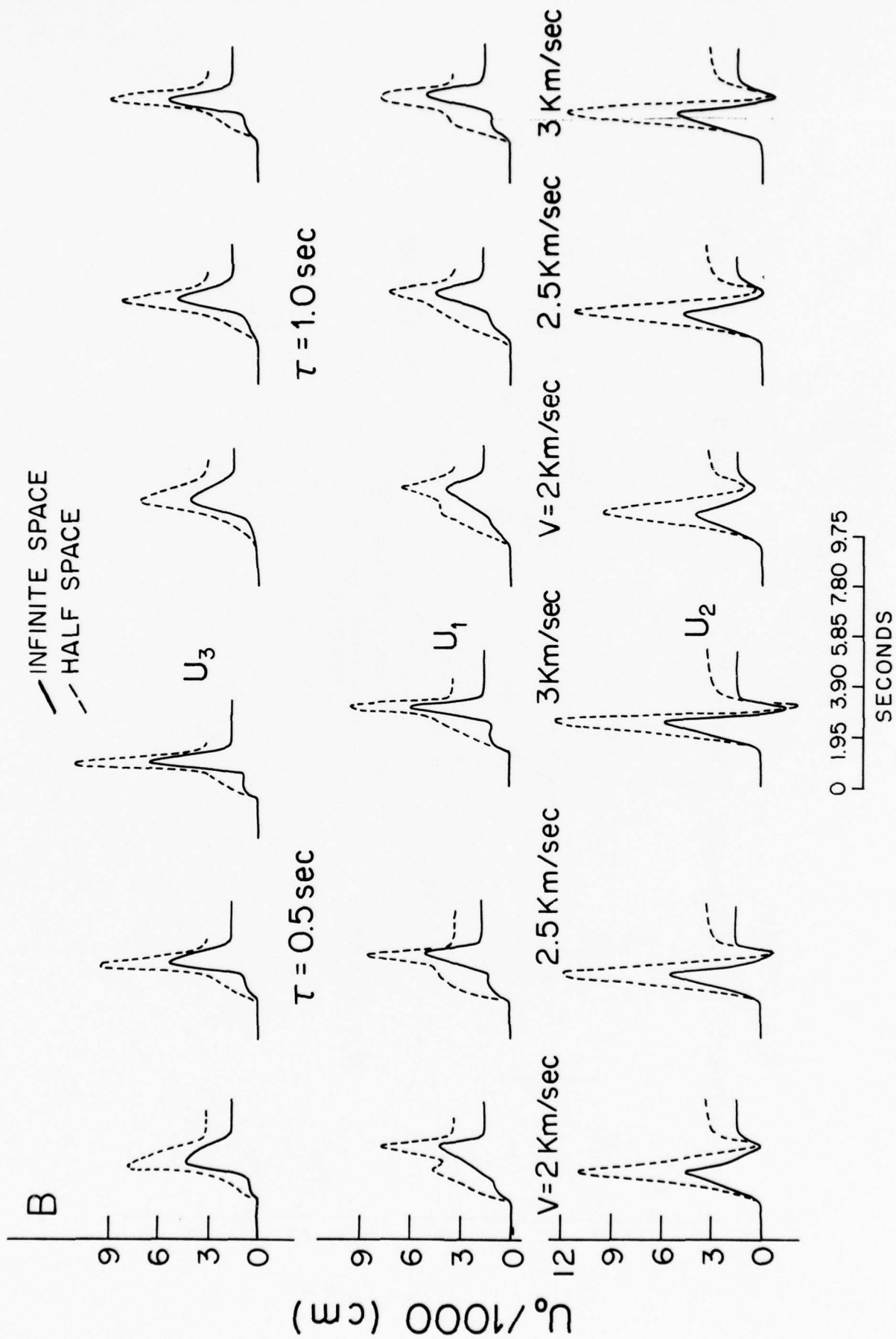


FIGURE 4

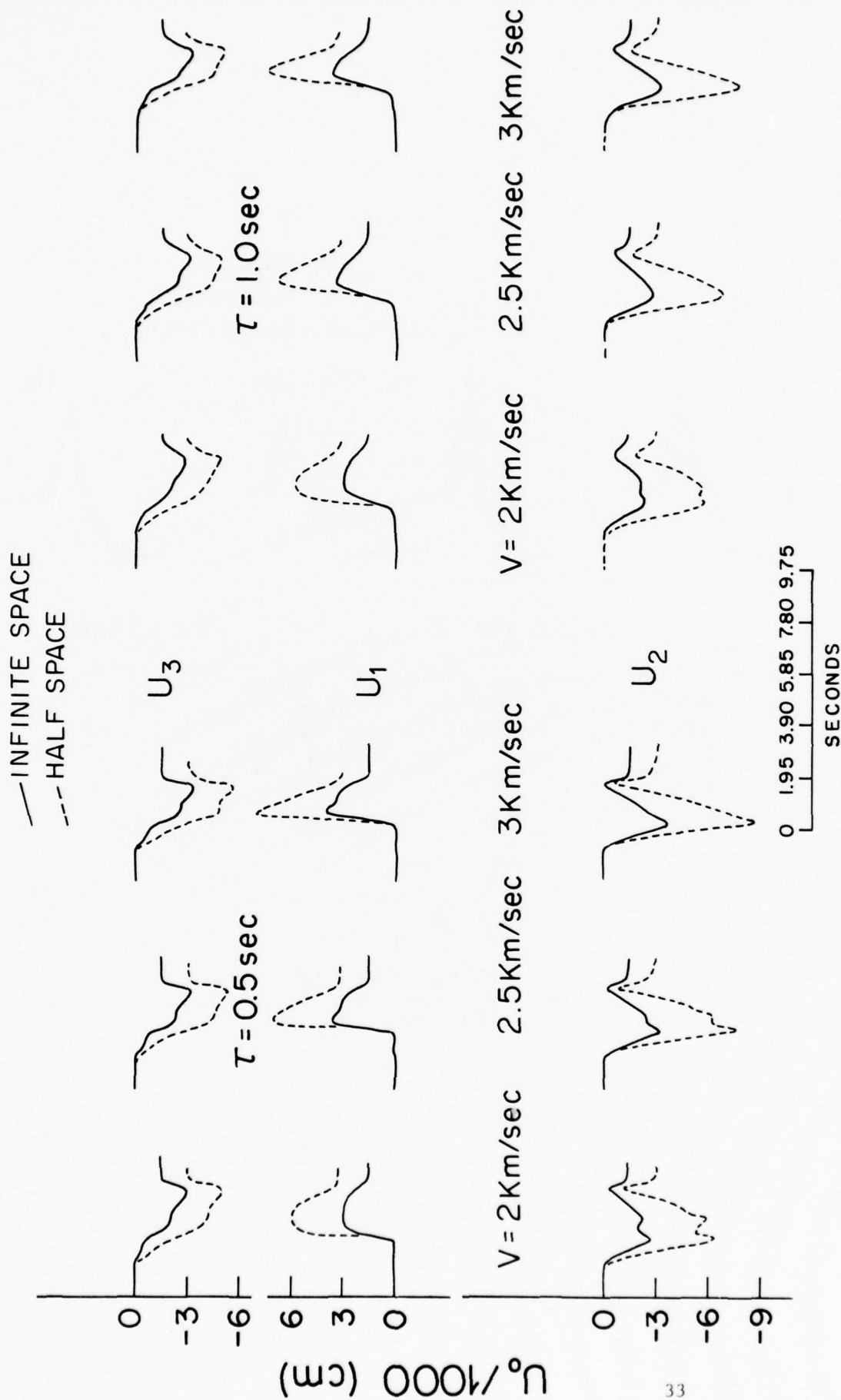


FIGURE 5

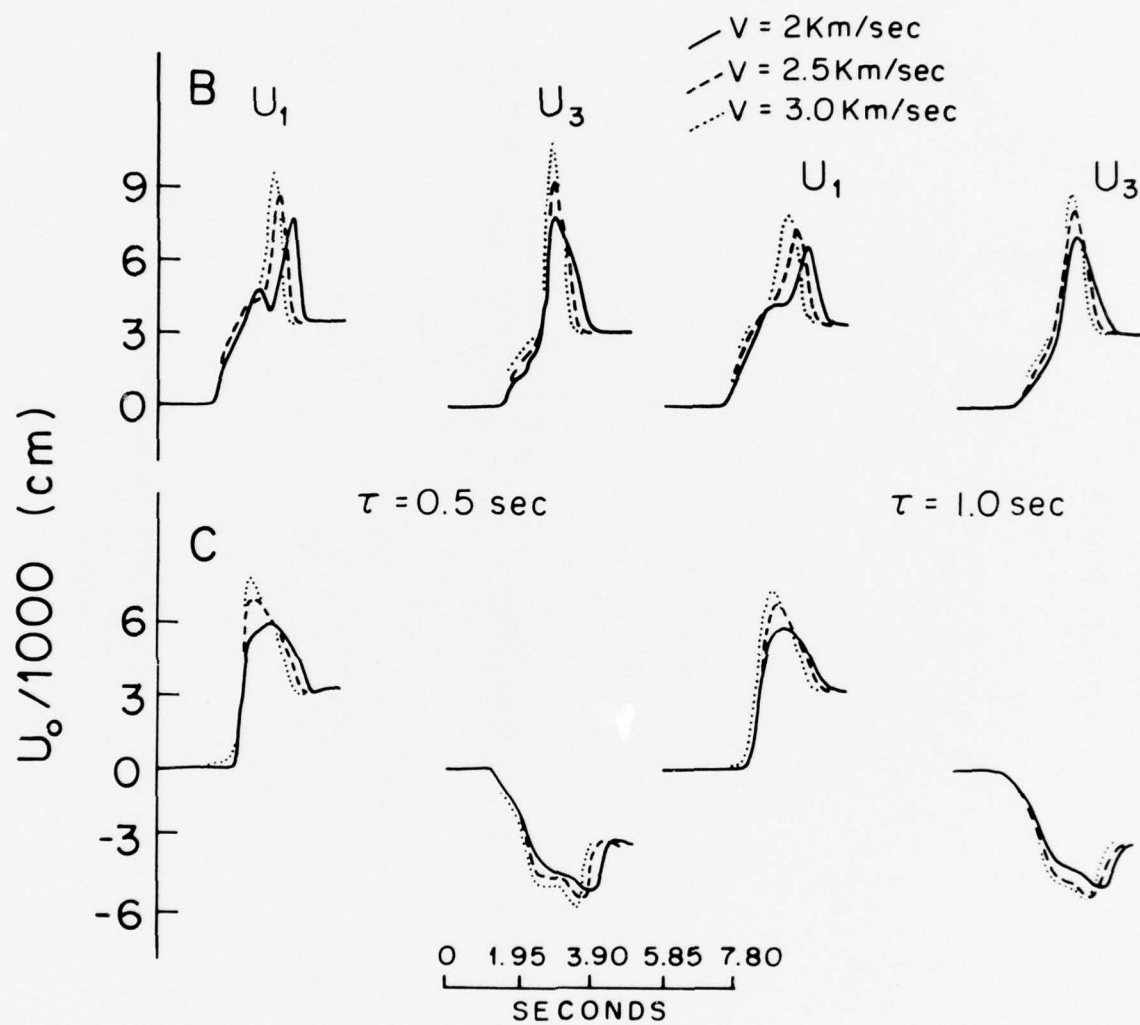


FIGURE 6

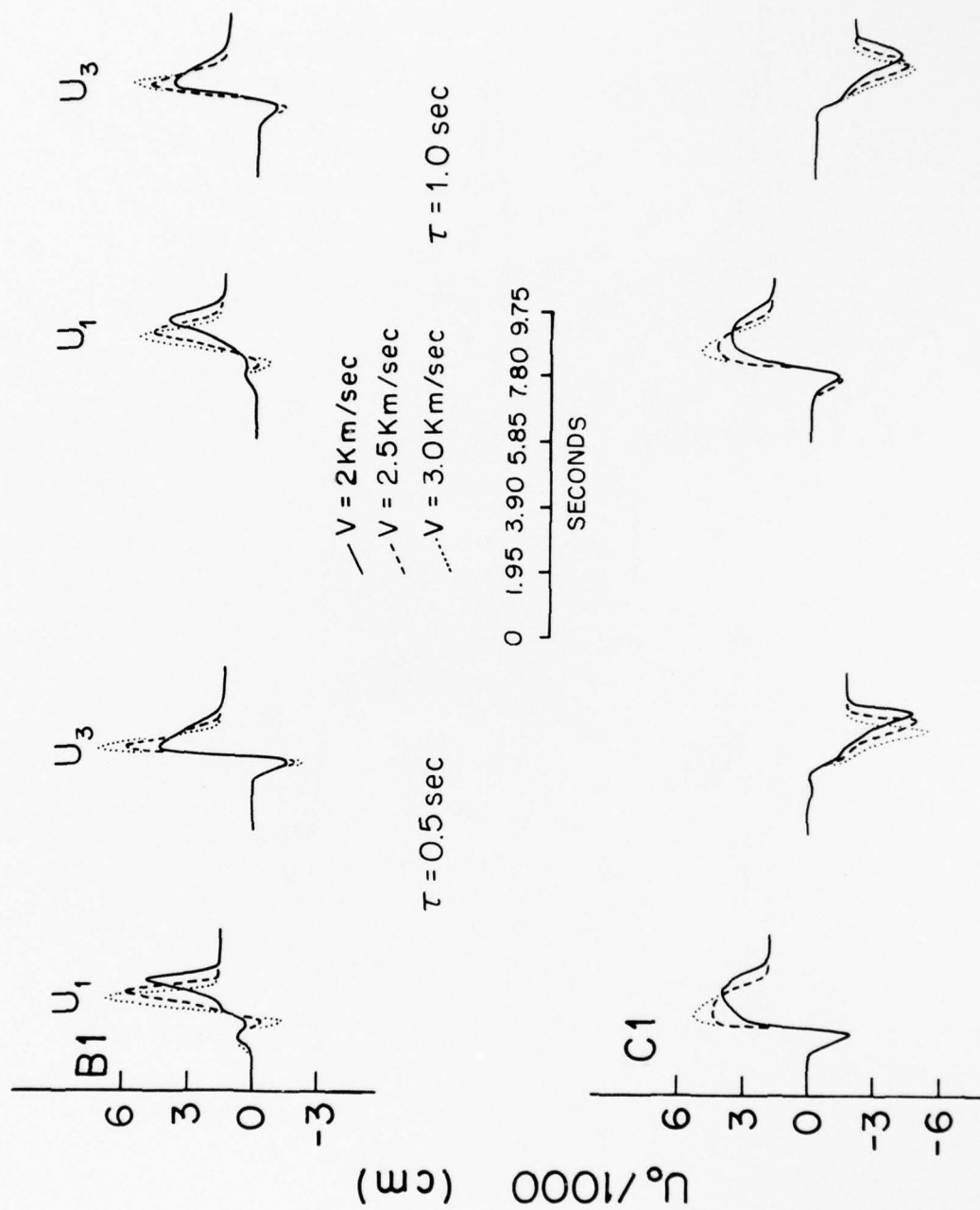


FIGURE 7

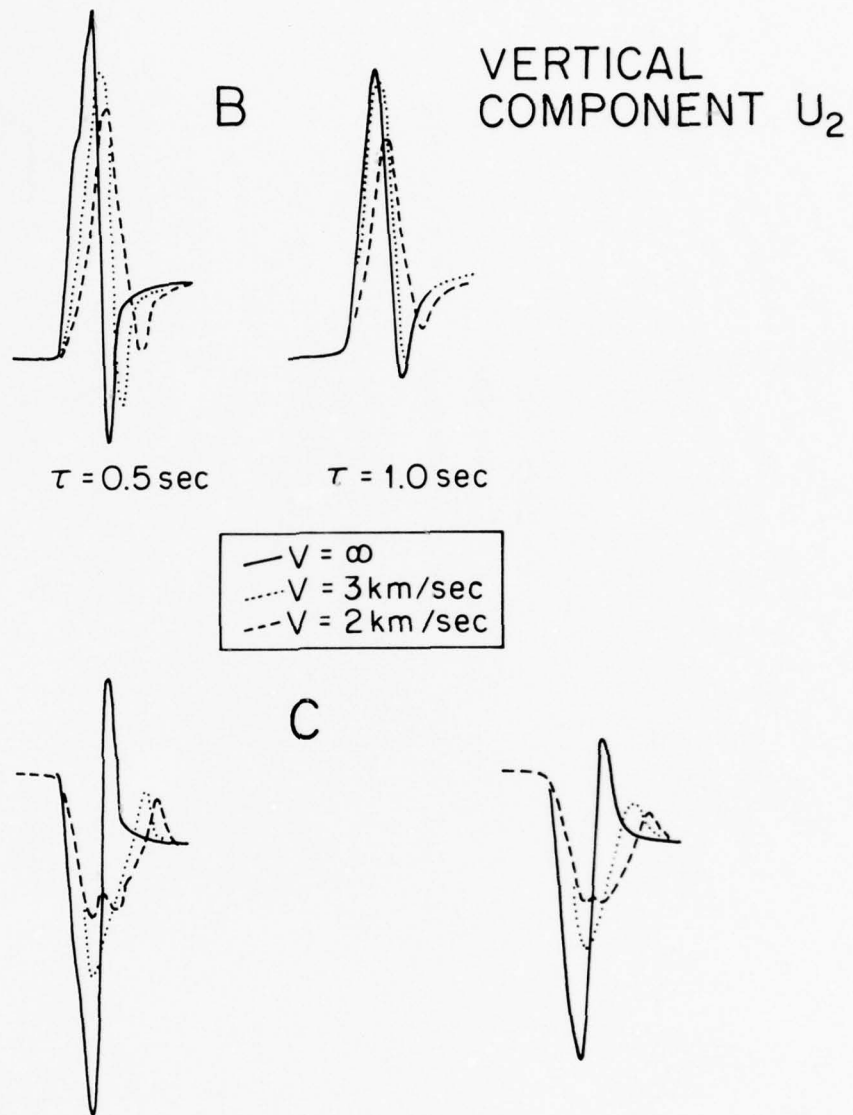


FIGURE 8

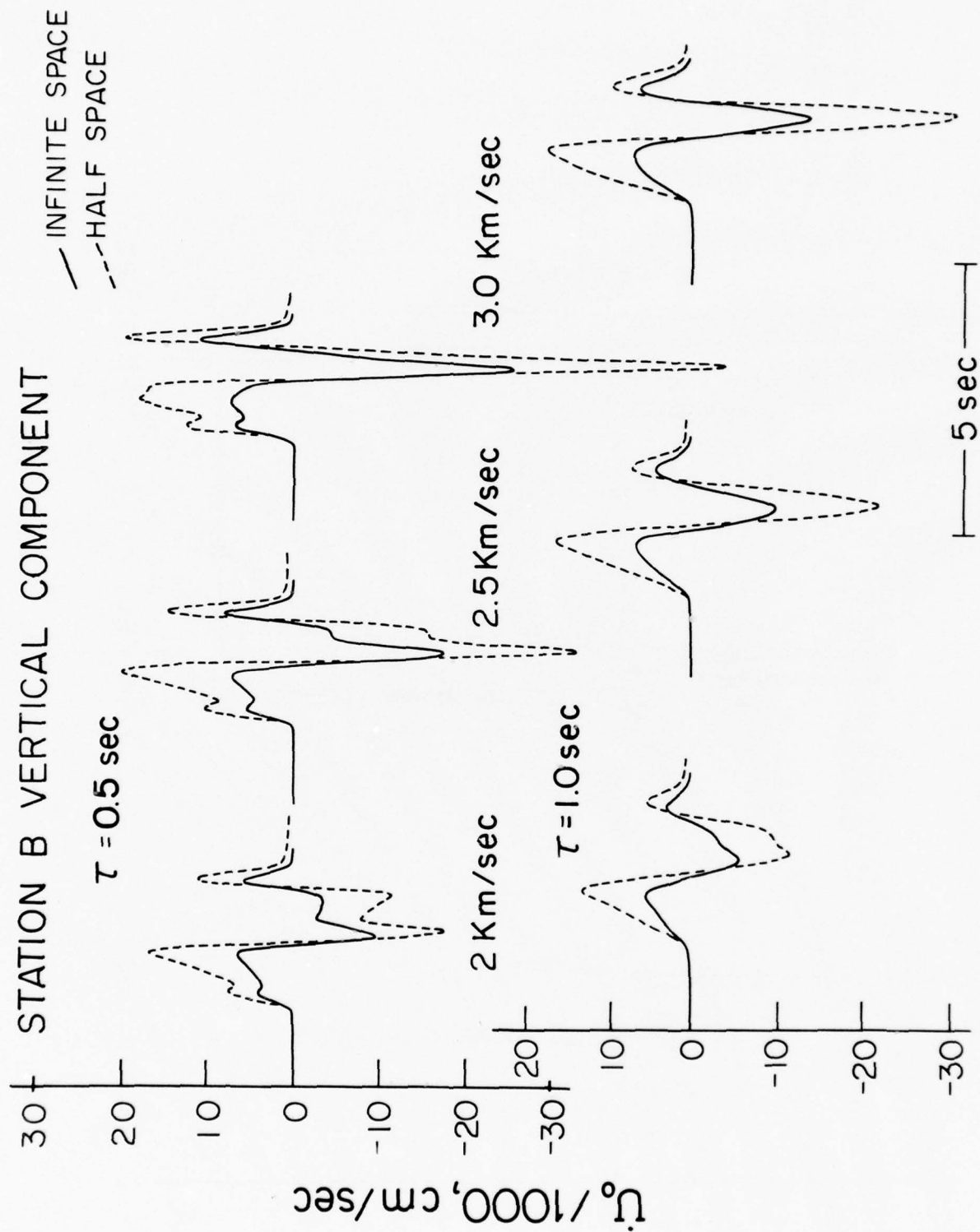


FIGURE 9

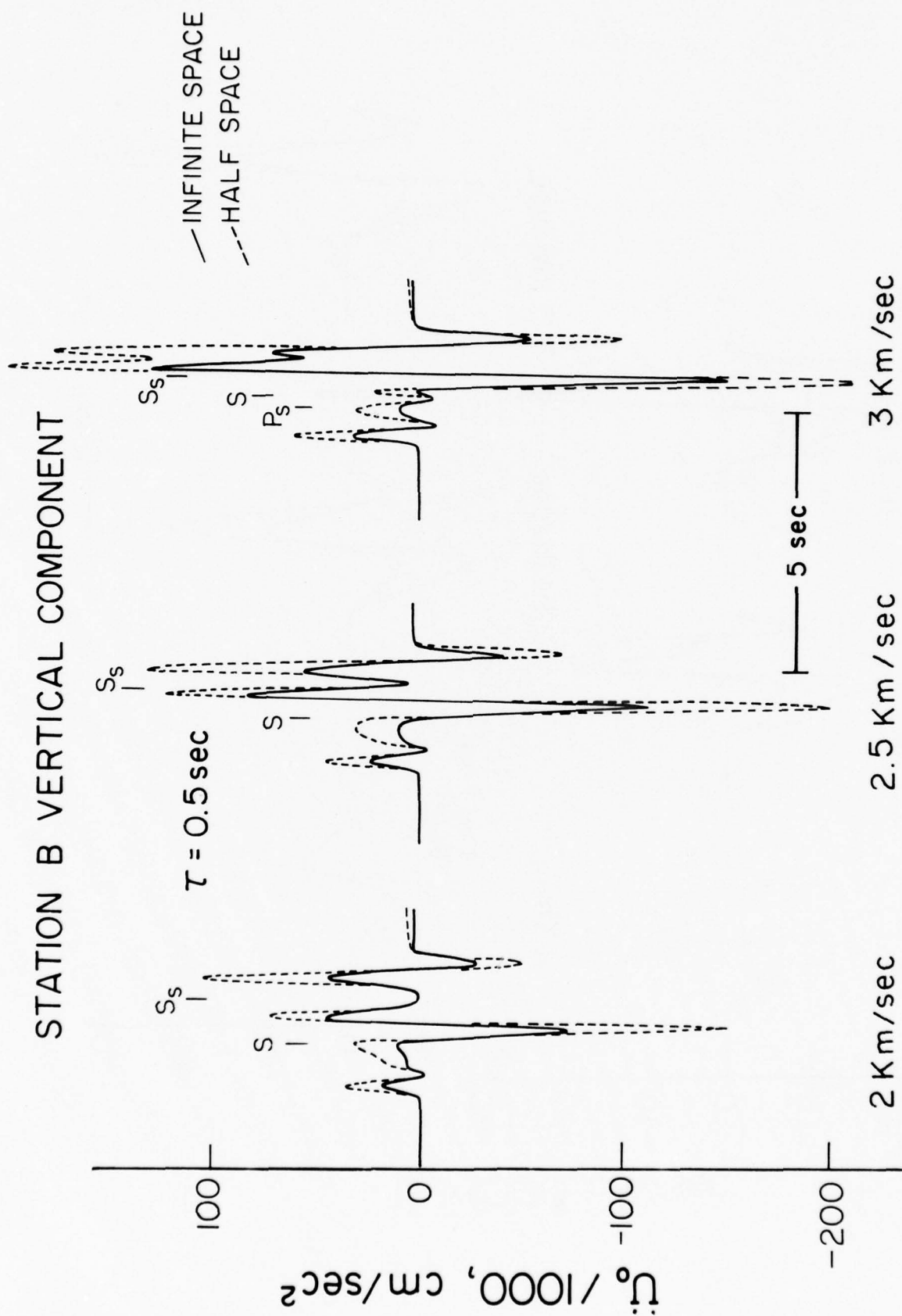


FIGURE 10

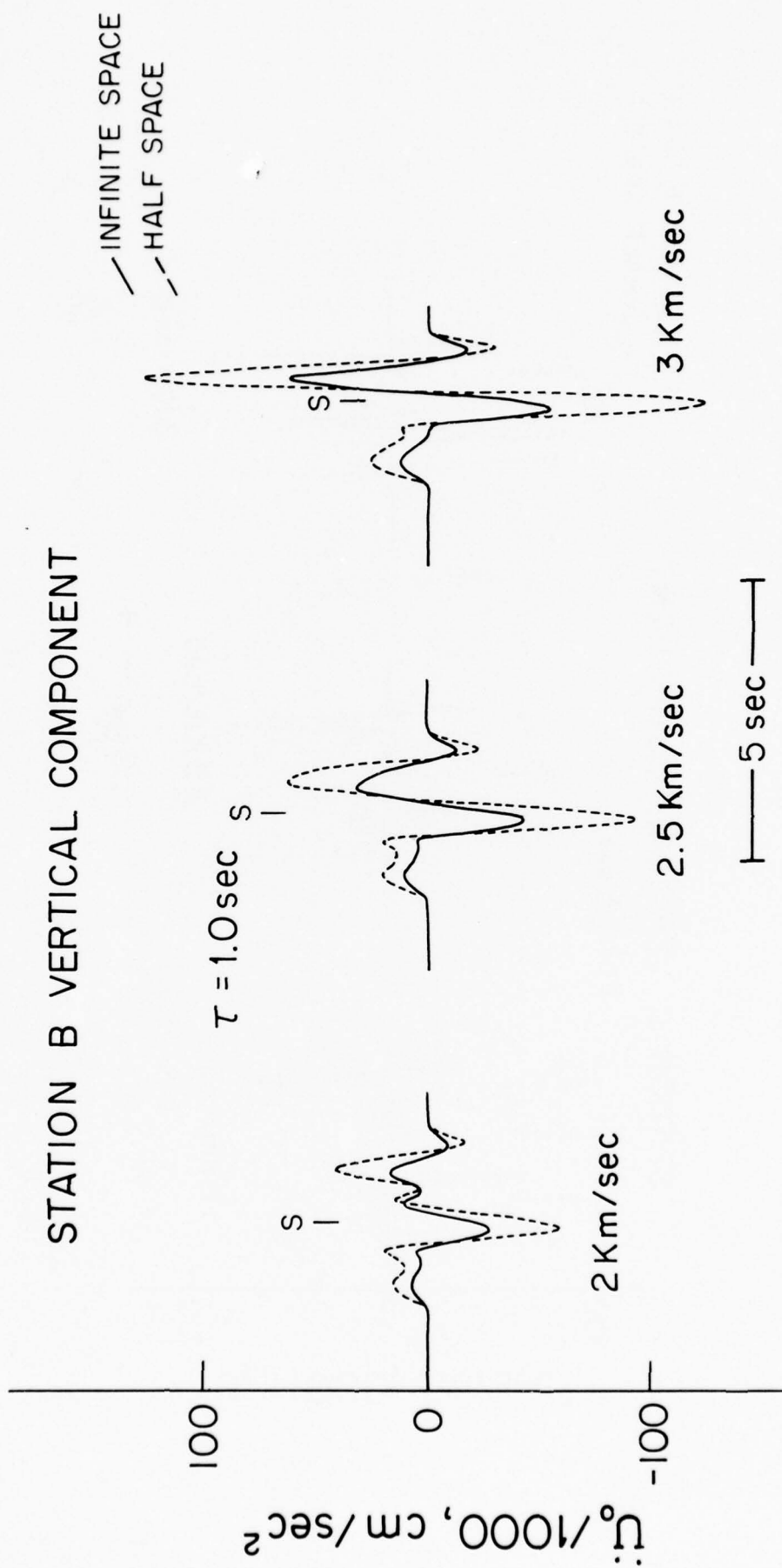


FIGURE 11

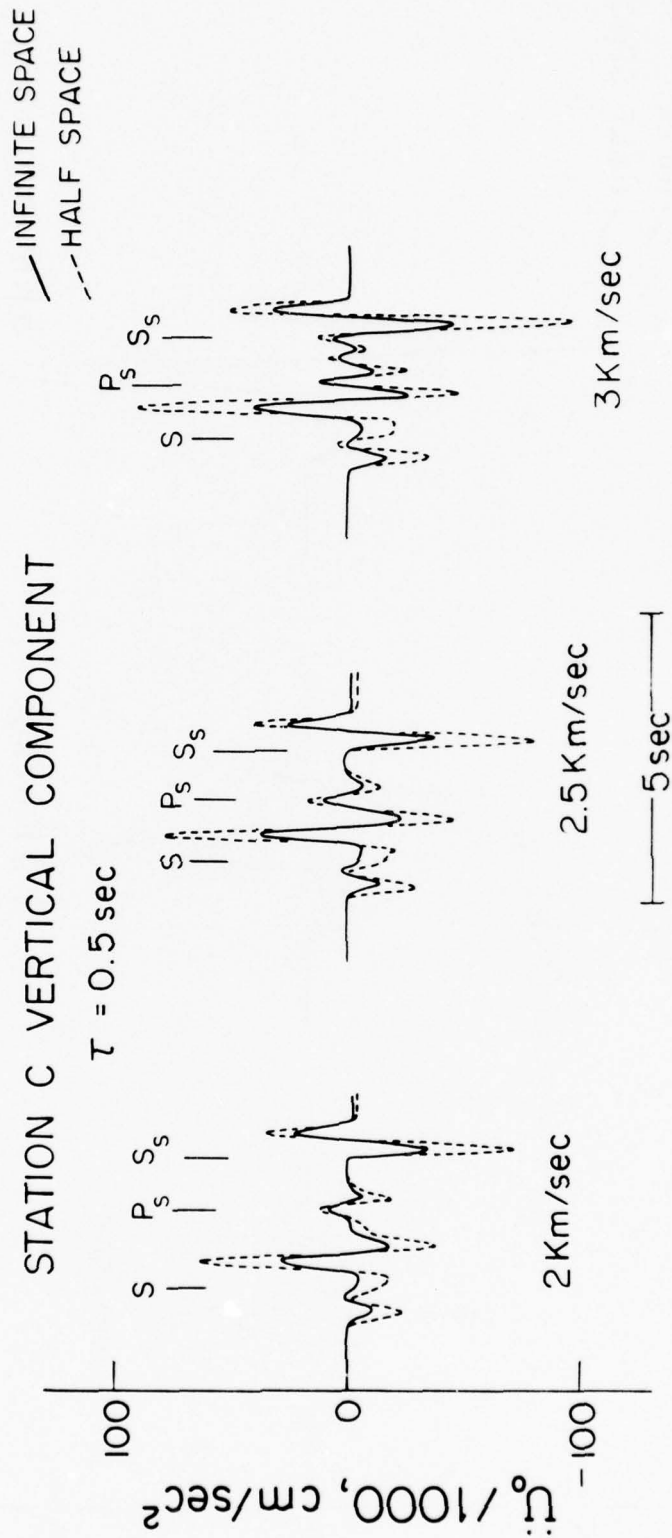


FIGURE 12

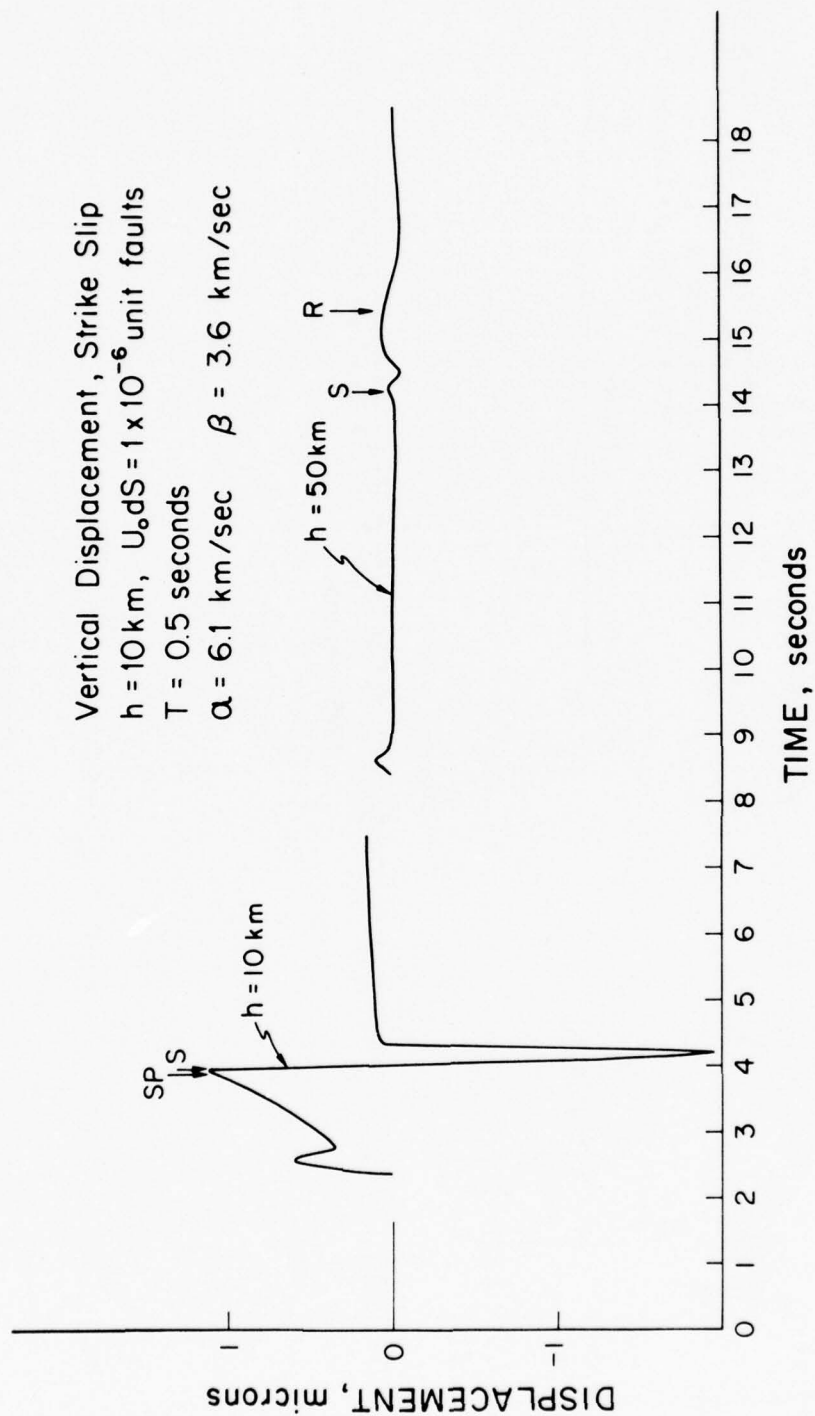


FIGURE 13

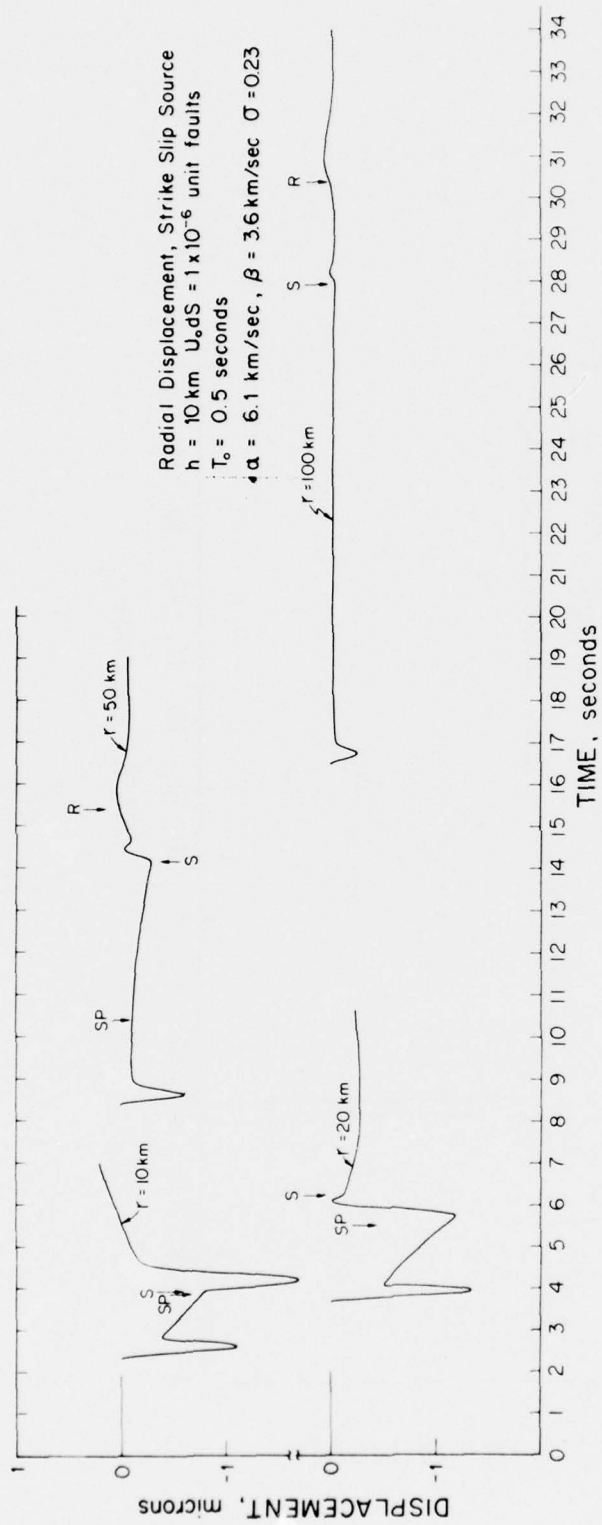


FIGURE 14

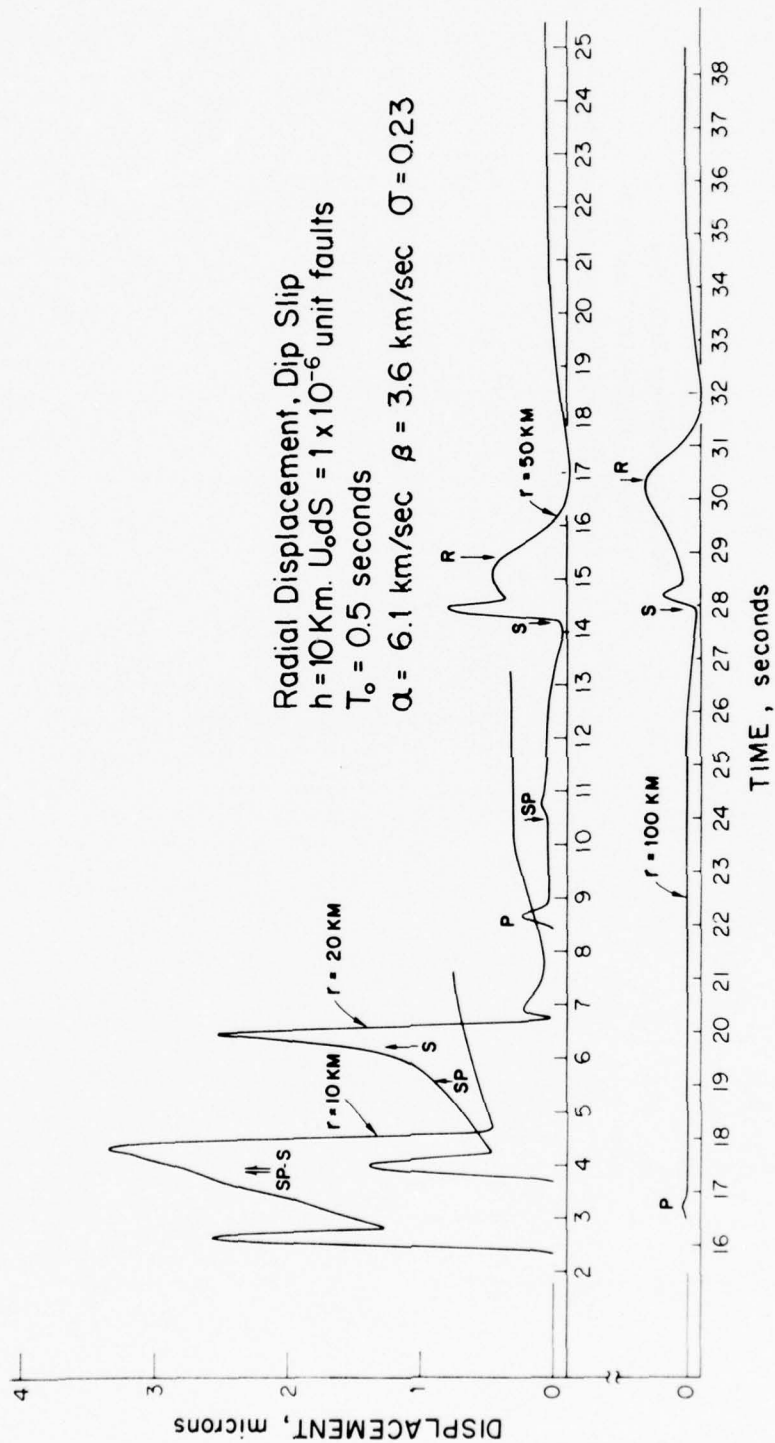


FIGURE 15

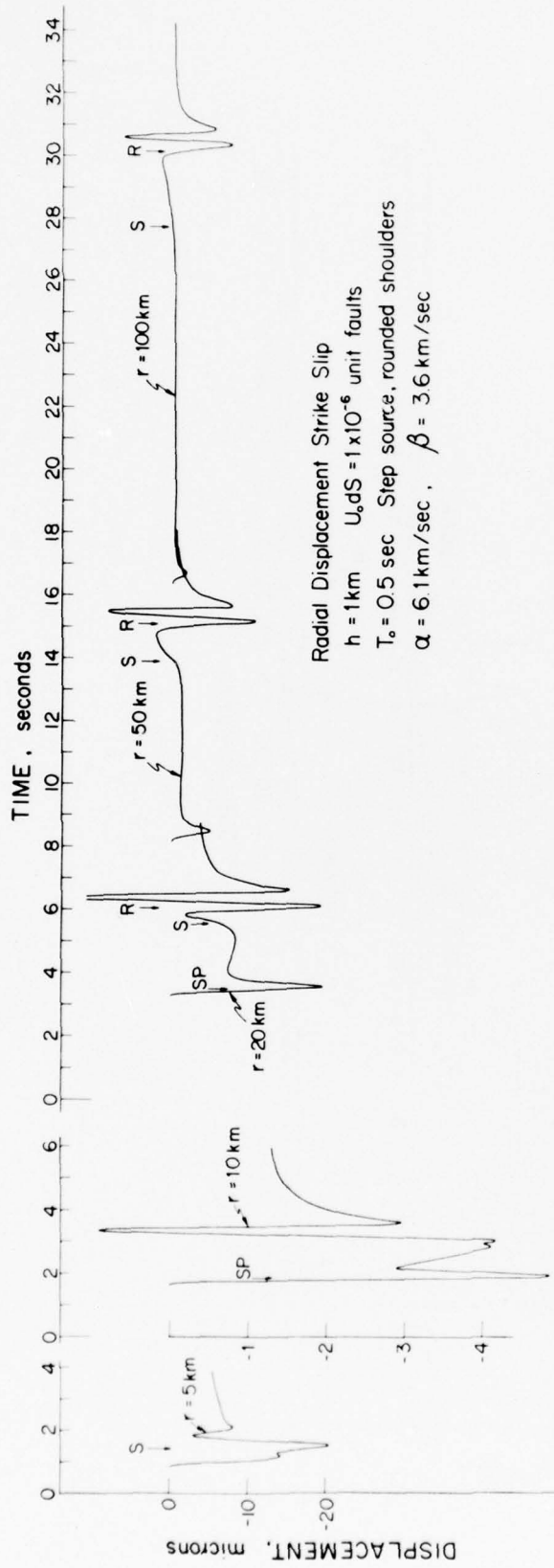


FIGURE 16

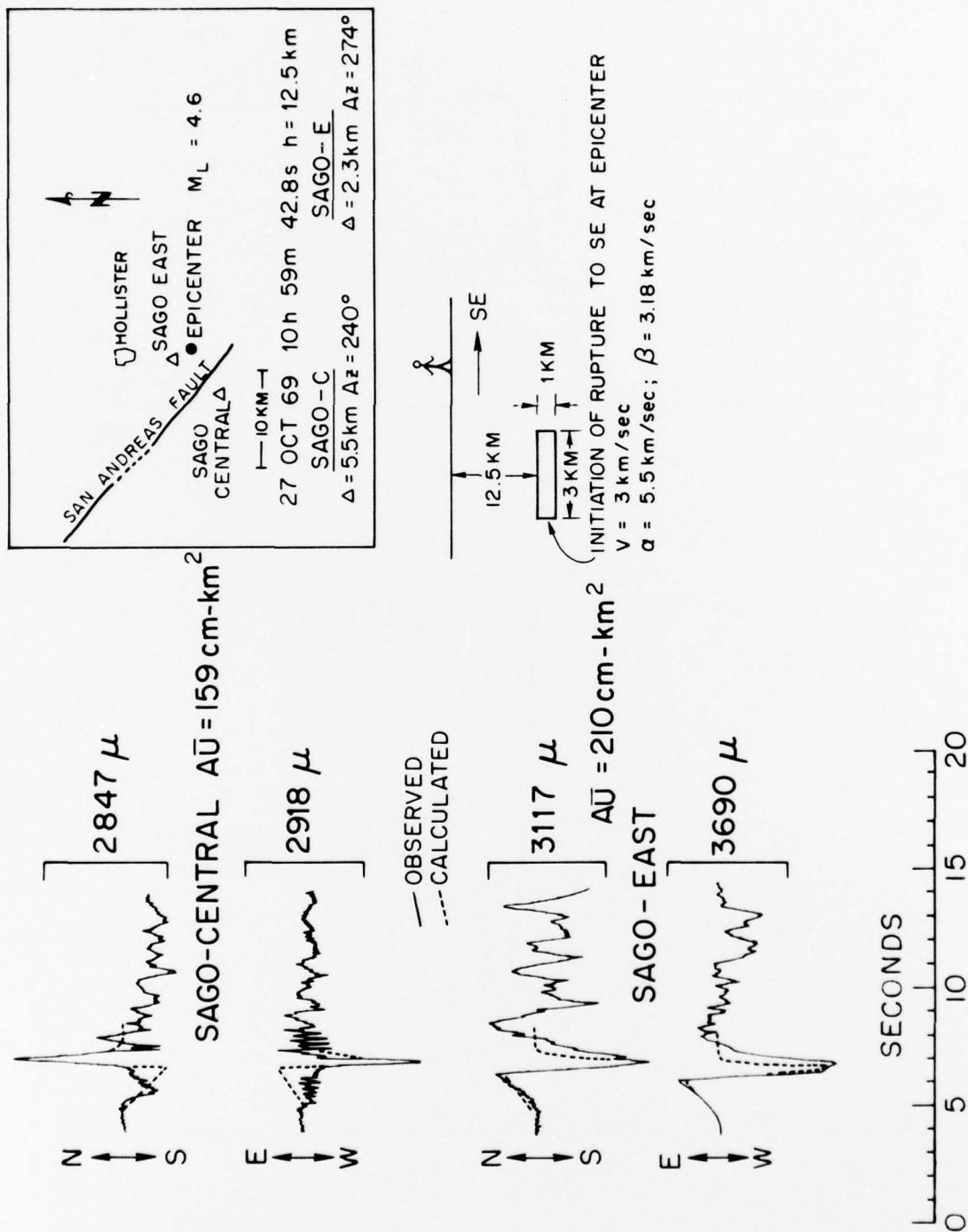


FIGURE 17

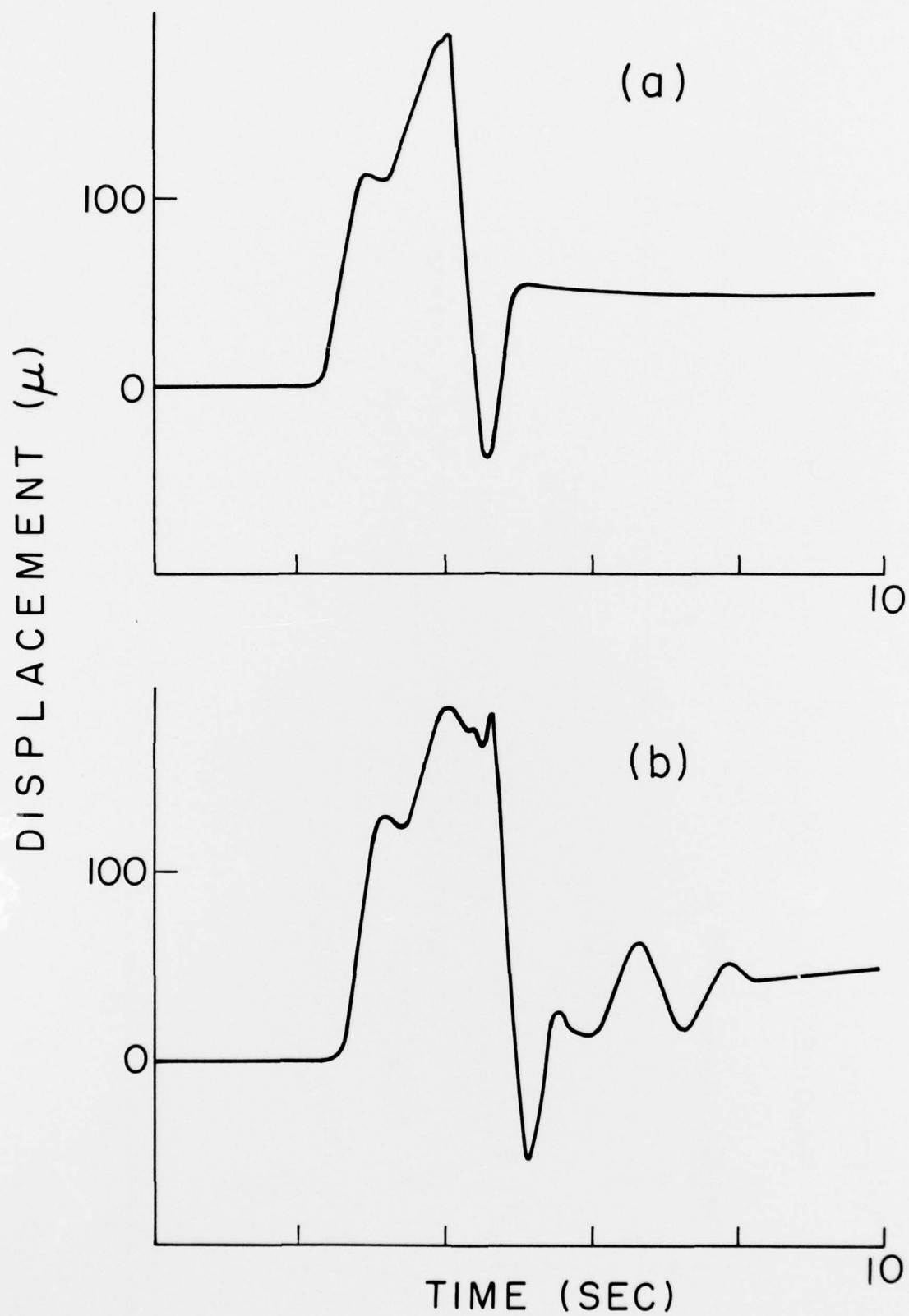


FIGURE 18

APPENDIX A

SAMPLE COMPUTER LISTING

There are two programs to compute the vertical component of motion for a propagating strike-slip fault. Program one should be submitted first, the numerical results of this program being stored on disc. This information is used when program two is submitted. The programs are used to compute ground displacements, velocities or accelerations. The source may be either a line source or a rectangular source. Computations may be done for an infinite or half space model.

The most time consuming computations are the functions u_{z,p_1} , u_{z,s_1} , (see eqns. (15), (16)). Program one computes the numerical values of these functions once and for all. The values of $u_{z,p_1} + u_{z,s_1}$ are stored on disc for all subrectangular sources required. Program two uses these values several times to compute the acceleration, velocity, or displacement, for any required rise time or rupture velocity.

PROGRAM ONE

INPUT (see figure 1)

ALFA: P velocity (km/sec)

BETA: S velocity (km/sec)

H: Source depth in km (depth to top of fault plane)

D: Horizontal range in km

DT: time increment in $u_{z,p_1} + u_{z,s_1}$ computations.

Time: the required computational time of ground motion (sec)

E^{++} : the absolute permitted error in u_{z,p_1}, u_{z,s_1}

EE^{++} : the relative permitted error in (same as above)

DELH: fault width (km)

DELX: fault length (km)

PHI: azimuth to station in degrees (see figure 1)

NH: number of subrectangles required

INDX1: 1 denotes a half space model; 2 an infinite space model

INDX2: 1 denotes a rectangular source; 2 a line source at depth
H, length DELX.

OUTPUT

1/ Arrivals time of P, SP, S from depth H and H + DELH for all
subrectangles.

2/ The numerical values of $u_{z,p_1} + u_{z,s_1}$ for all rectangles.
These values are printed and stored on the disc in unit 8.

$^{++}$ The error less than the absolute error or the relative error.

PROGRAM TWO

INPUT

NV: The number of different rupture velocity cases to be computed.

INDEX: 1 for displacement ground motion, 2 for velocity ground motion, and 3 for acceleration.

TZ: rise time in seconds (2 in equation (21))

VZ: the first value in rupture velocity (km/sec)

DV: increment in rupture velocity

OUTPUT

A/ The values of rupture velocity and rise time are printed as well as the values of ground motion. Displacement amplitude is given in terms of U_0 , velocity in terms of $U_0/(\text{sec})$, and acceleration in terms of $U_0/(\text{sec}^2)$.

B/ A plot for each required rupture velocity. The values of displacements, velocities and accelerations were multiplied by 1000 before plotting.

PROGRAM ONE

```

C      PROGRAM TO COMPUTE SURFACE MOTION OF HALFSPACE , DUE TO BURIED
C      SOURCE VERTICAL MOTION
      IMPLICIT REAL*8 (A-H,O-Z)
      DIMENSION Q(1008),QS(1008),QQ(1008),QK(1008)
      COMMON/PLQ/Q, QS,DT,TZ
      COMMON/PP1/ALFA,BETA, TIME,E,EE,IPL0T
      COMMON/AAA/INDX1,INDX2
      READ 70,ALFA,BETA,H,D,DT,TIME,E,EE
      READ 70,DELH,DELX,PHI
      READ 73,NH
      READ 73,INDX1,INDX2
      PRINT 104,ALFA,BETA,H,D,DT,TIME,E,EE
      PRINT 74,DELH,DELX,PHI
      PRINT 75,NH
      PRINT 75,INDX1,INDX2
70  FORMAT(8F10.5)
73  FORMAT(3I5)
      DO 207 I=1,1000
207  Q(I)=0.
      H=H+DELH/2.00
      WRITE(8) H,D,DT,TIME,DELH,DELX,PHI
      WRITE(8) NH,ALFA,BETA
74  FORMAT(1X,5E15.7)
      PI=DARCOS(-1.00)
      PHI=PHI*PI/1.802
      D1=D
      RNS=D1*D1
      RS=RNS+(H-DELH/2.00)*(H-DELH/2.00)
      R=DSQRT(RS)
      T1=R/ALFA
      IP=T1/DT+1
      NI=TIME/DT+IP
75  FORMAT(1X,5I3)
      H1=H
      ANH=NH
      DXT=1.00/ANH
      ALC=0.00
      TS=0.
      DO 27 II=1,NH
      AII=II
      TS=TS+DXT
      AL=DELX*(TS)
      ST=AL-ALC
      SP=(AL+ALC)/2.00
      ALC=AL
      RNS=D1*D1+SP*SP-2.00*D1*SP*DCOS(PHI)
      DIM=DSQRT(RNS)
      H=H1+1.500*DELH
      IF(INDX2.EQ.2)H=H1+0.500*DELH
      D=DIM
      MNH=2

      IF(INDX2.EQ.2)MNH=1
      DO 2 I=1,1008
2  QQ(I)=0.00
      DO 1 J=1,MNH
      AJ=-1.
      IF(INDX2.EQ.2)AJ=1.
      IF(J.EQ.2)AJ=1.
      H=H-DELH
301  CALL VRM(H,D,NI)
      DO 1 I=1,1008
      QQ(I)=QQ(I)+Q(I)*AJ
1  CONTINUE
      DO 3 I=1,1008
3  Q(I)=QQ(I)
      WRITE(8) (Q(I),I=1,NI)
      PRINT 104,(Q(I),I=1,NI)
27  CONTINUE
104  FORMAT(2X,10E12.4)
      STOP
      END

```

```

SUBROUTINE VRM(H,DIM,NI)
IMPLICIT REAL*8 (A-H,O-Z)
EXTERNAL FUNP ,FUNS ,FUNSP ,FUNSS
DIMENSION Q(1008) ,QS(1008),QS2(1008),QS3(1008)
COMMON/PLO / Q,QS,DT,TZ
COMMON HR2,DR2,SA,SB,SC,RA,RB,TBP,TBS,D ,T ,TBSR
COMMON/PP1/ALFA,BETA, TIME,E,EE,IPL0T
COMMON/AAA/INDX1,INDX2

C
D=DIM
DO 999 I=1,1008
Q(I)=0.D0
QS1(I)=0.D0
QS2(I)=0.D0
QS3(I)=0.C0
999 QS(I)=0.D0
PIK=0.5D0*CARCOS(-1.D0)
PRINT 73,H,D
73 FORMAT(30X,'VERTICAL DISPLACEMENT',/, 18X,'SOURCE DEPTH ',F8.3,
1 'KM . HORIZONTAL RANGE ',F8.3,' KM.')
RS= H*H+D*D
DR2=D/RS
HR2=H/RS
R =DSQRT(RS)
FA =1.00/ALFA
EB =1.00/BETA
SA = FA*FA
SB = EB*EB
HCR=H/DSQRT(SB/SA-1.D0)
SC = 0.5*SB
RA = RS*SA
RB = RS*SE
TBP =R*FA
PRINT 74,TBP
74 FORMAT(18X,'P ARRIVAL TIME ',F10.5 ,' SEC.')
IP =TBP/DT +1
TB =IP*DT
T= TB-DT
N=NI
DO 1 I=IP,N
T=T+DT
1 Q(I)=QUAD(0.D0,PIK,FUNP,E,EE,4)
TBSR =R*EB
TBSH =D*FA +H*DSQRT(SB-SA)
IF(INDX1,EQ,2) GO TO 3
IF(D-HCR) 3,3,4
3 TBS =TBSR
75 FORMAT(18X,'NO SP HEAD WAVE. S ARRIVAL TIME ',F10.5,' SEC.')
PRINT 75,TBSR
IS = TBS/DT +1
J = IS-IP +1

TS=IS*DT
T = TS-DT
DO 2 I=IS,N
T=T+ DT
2 Q(I)= QUAD(0.D0,PIK, FUNS,E,EE,4)
Q(I)=Q(I)+QS(I)
GO TO 10
4 TBS =TBSH
PRINT 76,TBSH,TBSR
76 FORMAT(18X,' SP HEAD WAVE ARRIVAL TIME ',F10.5,' SEC. S ARRIVAL TI
ME ',F10.5,' SEC')
IS = TBS/DT +1
TS=IS*DT
J = IS-IP +1
T = TS-DT
PDRH=DARSIN (DSQRT(TBSH/TBSR) )
DO 18 I=IS,N
T=T+DT
IF(T.GT.TBSR) GO TO 9
PCRH=DARSIN (DSQRT(TBSH/T) )
QS1(I)=QUAD(PCRH,PIK,FUNSP,E,EE,4)
Q(I)=Q(I)+QS1(I)
GO TO 18
9 QS2(I)=QUAD(0.D0,PIK,FUNS,E,EE,4)
QS3(I)=QUAD(PDRH,PIK,FUNSS,E,EE,4)
Q(I)=Q(I)+QS3(I)+QS2(I)
18 CONTINUE
10 FACTOR=1.
RETURN
END

```



```

FUNCTION FUNP(X)
IMPLICIT REAL*8 (A-H,O-Z)
COMPLEX*16 C,V,VR,VSQ,P,TVR,D,VR2,AV2,BV2,CDSQRT
COMMON HR2,DR2,SA,SB,SC,RA,RB,TBP,TBS,RANGE,TT
COMMON/AAA/INDX1,INDX2
C=(0.00,1.00)
T=TT-(TT-TBP)*DSIN(X)**2
C
  IN THIS SUB T MEANS TAU
  A= T*T-RA
  IF(A.LT.0.00) A=0.00
  A= DSQRT(A)
  V=DR2*T+HR2*A*C
  VSQ= V *V
  P =SC - VSQ
  AV2=SA-VSQ
  BV2=SB-VSQ
  VR=V*RANGE
  DT=TT-T
  TVR=DT+VR+VR
  DT=DT+DT
  VR2=VR*VR
  D=CDSQRT(AV2)
  C=D
  IF(INDX1.EQ.2) GO TO 1
  D=V*P/D/((P*P+VSQ*D*CDSQRT(BV2))*CDSQRT(TVR*(T+TBP)))*(DT*TVR+VR2)
  GO TO 2
1 D=V*D / (SB
  *CDSQRT(TVR*(T+TBP)))*(DT*TVR+VR2)
2 IF(INDX2.EQ.1) D=D/C
  FUN=D
  FUNP =FUN
  RETURN
  END

```

```

FUNCTION FUNS(X)
IMPLICIT REAL*8 (A-H,O-Z)
COMPLEX*16 C,V,VR,VSQ,P,TVR,D,VR2,AV2,BV2,CDSQRT
COMMON HR2,DR2,SA,SB,SC,RA,RB,TBP,TBS,RANGE,TT,TBSR
COMMON/AAA/INDX1,INDX2
C=(0.00,1.00)
T=TT-(TT-TBSR)*DSIN(X)**2
A= T*T-RB
IF(A.LT.0.) A=0.00
A= DSQRT(A)
C
  IN THIS SUB T MEANS TAU
  V=DR2*T+HR2*A*C
  VSQ= V *V
  P =SC - VSQ
  AV2=SA-VSQ
  BV2=SB-VSQ
  VR=V*RANGE
  DT=TT-T
  TVR=DT+VR+VR
  DT=DT+DT
  VR2=VR*VR
  D=CDSQRT(AV2)
  C=CDSQRT(BV2)
  IF(INDX1.EQ.2) GO TO 1
  D=-V*B*V2*(DT*TVR+VR2)*D/((P*P+VSQ*D*CDSQRT(BV2))*CDSQRT(TVR*(T+
  *TBSR)))
  GO TO 2
1 D=-V*C *(DT*TVR+VR2) / (SB
  *CDSQRT(TVR*(T+
  *TBSR)))
2 IF(INDX2.EQ.1) D=D/C
  FUN=D
  FUNS =FUN
  RETURN
  END

```

```

FUNCTION FUNSP(X)
  IMPLICIT REAL*8 (A-H,O-Z)
  COMPLEX*16 AV2,D,CDSQRT
  COMMON      HR2,DR2,SA,SB,SC,RA,RB,TBP,TBS,RANGE,TT ,TBSR
  COMMON/AAA/INDX1,INDX2
  T=TT      *DSIN(X)**2
  A= T*T-RB
  A=DSQRT(-A)
C   IN THIS SUB  T MEANS TAU
  V=DR2*T-HR2*A
  VSQ= V *V
  P  =SC - VSQ
  AV2=SA-VSQ
  BV2=SB-VSQ
  VR=V*RANGE
  DT=TT-T
  TVR=DT+VR+VR
  DT=DT+DT
  VR2=VR*VR
  D=CDSQRT(AV2)
  D=V*BV2*(DT*TVR+VR2)*D* DSQRT(T/(TVR*(T+TBSR)*(TBSR-T)))/(P*P+VSQ*
  *D*CDSQRT(BV2*(1.D0,0.D0)))
  IF(INDX2.EQ.1) D=D/CDSQRT(BV2*(1.D0,0.D0))
  FUN=D*(0.D0,-1.D0)
  FUNSP= FUN
  RETURN
  END

```

```

FUNCTION FUNSS(X)
  IMPLICIT REAL*8 (A-H,O-Z)
  COMPLEX*16 AV2,D,CDSQRT
  COMMON      HR2,DR2,SA,SB,SC,RA,RB,TBP,TBS,RANGE,TT,TBSR
  COMMON/AAA/INDX1,INDX2
  T=TBSR      *DSIN(X)**2
  A= T*T-RB
  A=DSQRT(-A)
C   IN THIS SUB  T MEANS TAU
  V=DR2*T-HR2*A
  VSQ= V *V
  P  =SC - VSQ
  AV2=SA-VSQ
  BV2=SB-VSQ
  VR=V*RANGE
  DT=TT-T
  TVR=DT+VR+VR
  DT=DT+DT
  VR2=VR*VR
  D=CDSQRT(AV2)
  D=V*BV2*(DT*TVR+VR2)*D* DSQRT(T/(TVR*(T+TBSR)*(TT -T)))/(P*P+VSQ*
  *D*CDSQRT(BV2*(1.D0,0.D0)))
  IF(INDX2.EQ.1) D=D/CDSQRT(BV2*(1.D0,0.D0))
  FUN=D*(0.D0,-1.D0)
  FUNSS= FUN
  RETURN
  END

```

```

FUNCTION QUAD(A,B,FUN,EPS,ETA,MIN)
IMPLICIT REAL*8 (A-H,O-Z)
DIMENSION Q(16)
H=B-A
FCNA =FUN(A)
FCNB =FUN(B)
TABS =DABS(H)*(DABS(FCNA)+DABS(FCNB)) *0.5
T      =      H *(      FCNA +      FCNB ) *0.5
NX      =1
DO 12 N=1,15
H=H*0.5
SUM=0.00
SCORR=0.00
SUMABS=0.00
DO 2 I=1,NX
XI=2.* DFLQAT(I)-1.
FCNXI = FUN(A+XI*H)
SUMABS=SUMABS+ DABS(FCNXI)
FCNXI = FCNXI + SCORR
SS = SUM +FCNXI
SCORR= SUM-SS + FCNXI
2 SUM=SS
T= T*0.5+H*SUM
TABS= TABS*0.5 +DABS(H)*SUMABS
Q(N)= 2.*(T+H*SUM)*0.33333333
IF(N-2) 10,3,3
3 F =4.
DO 4 J=2,N
I=N+1-J
F=F*4.
4 Q(I)=Q(I+1)+(Q(I+1)-Q(I))/(F-1.)
IF(N-3) 9,5,5
5 IF(N-MIN) 9,6,6
6 X= DABS(Q(1)-QX2)+DABS(QX2-QX1)
IF (TABS) 7,8,7
7 IF(X/TABS-3.*(DABS(ETA)+0.14901161D-7)) 11,11,8
8 IF( X-3.*DABS(EPS)) 11,11,9
9 QX1=QX2
10 QX2=Q(1)
12 NX=NX+NX
11 QUAD = Q(1)
RETURN
END

```

PROGRAM TWO

```

REAL*8 Q,QS,VZ,AS1,CDE,DT
COMMON/ SVPS/A(1008),C(1008)
COMMON/ SP/YP(1008),XP(1008),BUFF(200)
COMMON/ PP/AQ(1008)
COMMON/ PLC/Q,QS,DT,TZ
COMMON/ IN/INDEX
DIMENSION Q(1008),QS(1008)
READ 20,NV
READ 20,INDEX
PRINT 20,NV
PRINT 20,INDEX
20 FORMAT(2X,13)
READ 21,TZ,VZ,DV
PRINT 22,TZ,VZ,DV
21 FORMAT(6F10.5)
22 FORMAT(2X,6F10.5)
INIP=1
NV=NV+1
CALL MUSEG(BUFF,'MUSEG,BIN 524',13)
3 CONTINUE
CALL ME(VZ,NV)
DO 1 J=1,N
1 AQ(J)=QS(J)
PRINT 30,VZ,TZ
30 FORMAT(2X,'BURSTURE VELOCITY=',E12.4,'RISE TIME=',E12.4)
VZ=VZ+DV
N=N+1
PRINT 11,(AQ(L),L=1,N)
YMI=0.
YMA=149.
XMI=(INIP-1)*524
XMA=XMI+524
11 FORMAT(2X,10E12.4)
FAC=DT
CALL GRAP1(N,FAC,XMI,YMI,XMA,YMA)
INIP=INIP+1
IF (INIP.EQ.NV) GO TO 5
GO TO 3
5 CALL EXITG(BUFF)
STOP
END

```

```

SUBROUTINE ME(VZ,N)
  IMPLICIT REAL*8(A-H, J-Z)
  DIMENSION Q(1000), QS(1000), QQ(1000), QK(1000)
  COMMON/PLC/Q, QS, DT, TZ
  READ(3) F, D, DT, TIME, DELH, DELX, PHI
  READ(3) AN, ALFA, BETA
  PI=3.141592653589793
  PIR=PI/2.
  DPI=2.00*PI
  PHI=PHI*PI/1.602
  TZI=DELX/VZ
  DI=0
  FS=D1*D1+(F-DELH/2.00)*(F-DELH/2.00)
  F=DSQRT(FS)
  T1=F/ALFA
  IP=T1/DT+1
  NI=TIME/DT+IP
  DO 102 I=1,1000
102 QK(I)=0.00
  75 FORMAT(1X,5I5)
  ANH=AN
  DXT=1.00/ANH
  ALC=0.00
  TS=0.
  DO 27 II=1,NI
  AII=II
  TS=TS+DXT
  AL=DELX*TS
  ST=AL-ALC
  SP=(AL+ALC)/2.00
  AL=AL
  PHS=D1*D1+SP*SP-2.00*D1*SP*DCOS(PHI)
  DIM=DSQRT(PHS)
  D=DIM
  DO 2 I=1,1000
  2 QQ(I)=0.00
  READ(3) TC(I), I=1,NI
  FACTOR=0.250/(PIK*PIK*D*D)
  DO 72 I=1,NI
  72 Q(I)=Q(I)*FACTOR
  CALL CONV(NI)
  4 FORMAT(5D13.4)
  C=D1*D1-3F*SP-0.0
  C=C/(2.00*SP*D)
  PHI1=CARCOS(C)
  IF(PHI1.LT.0.00) PHI1=-PHI1
  CDEF=DSIN(2.00*PHI1)*ST
  AN= TZI*(AII-1.00)/ANH
  AN=AN/DT
  NI1=AN
  DO 20 I=1,NI

```



```

SUBROUTINE GRAP1(N,FAC,XMI,YMI,XMA,YMA)
COMMON/SP/YP(1008),XP(1008),BUFF(200)
COMMON/PP/AQ(1008)
DT=FAC
T=0.
DO 700 I=1,N
XP(I)=T
700 T=T+DT
DO 200 J=1,N
200 YP(J)=AQ(J)*1000.
BUFF(84)=1.
BUFF(132)=1.
BUFF(177)=1.
CALL OBJECC(BUFF,XMI,YMI,XMA,YMA)
CALL SUBJEG(BUFF,0.,-50.,8.,50.)
CALL GRAPHG(BUFF,N,XP,YP,1,'X',1,'Z',0,'X V SZ')
RETURN
END

```

```

SUBROUTINE SI(TZ,DT,N)
REAL*8 Q,CS,DTDB,TZDB
COMMON /PLC/ Q,CS,DTDB,TZDB
COMMON/IN/INDEX
DIMENSION A(1008),Q(1008),QS(1008)
EQUIVALENCE (QS(1),A(1))
T=0.
PI=ARCCOS(-1.)
TPI=PI+PI
GM=TPI/TZ
DO 11 I=1,N
11 A(I)=0.
DO 1 I=1,N
IF(T.GT.TZ) GO TO 5
GO TO (20,21,22), INDEX
20 A(I)=(1.-COS(GM*T))/TZ
GO TO 1
21 A(I)=GM*SIN(GM*T)/TZ
GO TO 1
22 A(I)=GM*GM*COS(GM*T)/TZ
1 T=T+DT
5 CONTINUE
10 FORMAT(1X,12E10.2)
RETURN
END

```



```

SUBROUTINE CONV (N)
REAL*8 Q, QS, DTDB, TZDB
DIMENSION Q(1008), QS(1008), B(1000)
COMMON /PLC/ Q, QS, DTDB, TZDB
COMMON /SVSP/ A(1008), C(1008)
EQUIVALENCE (QS(1), B(1))
DATA AL, S, T/2., 3.14159, 0./
  DT=DTDB
  TZ=TZDB
DO 11 I=1, N
11 A(I)=C(I)
  CALL SI(TZ, DT, N)
  DO 1 K=1, N
    SUM=0.
    KK=K+1
    DO 2 J=1, K
      JJ=KK-J
2 SUM=SUM+B(J)*A(JJ)
1 C(K)=DT*(SUM-0.5*(B(1)*A(K)+B(K)*A(1)))
  DO 3 I=1, N
3 QS(I)=C(I)
  RETURN
  END

```